fire

MDPI

Article

Experimental Investigation on the Heat Dissipation and Postfire Structural Performance of a Reinforced Concrete Column with Biomimicked Geometry

M. Vishal * **and K.S. Satyanarayanan**

Department of Civil Engineering, SRM Institute of Science and Technology, College of Engineering and Technology, SRM Nagar, Kattankulathur-603203, Tamil Nadu, India
* Correspondence: vm8064@srmist.edu.in

Abstract: Cactus plants are prevalent in hot terrain locations. The spines in the cactus plants have an important function in preventing water evaporation. The strong pointed spines serve to distribute heat and prevent internal moisture loss owing to high heat. This paper addresses the biomimicking of a cactus plant to a reinforced concrete column. Columns are one of the most predominant elements in a structure and are responsible for maintaining the stability of the structure. Under the occurrences of fire, columns are the most affected, and the failure of the same could eventually steer to global collapse of the structure. In this study, various geometries were adopted based on the cactus plant, and the heat dissipation characteristics were studied. Finite element analysis was used to determine the optimal form based on the heat dissipation. The optimized shape was tested experimentally using a high-temperature localized heating element. Five column specimens were considered for experiments and named C (conventional nonheated column), C1 (conventional heated column), C2 (mimicked column), C3 (mimicked column with rebar in cone), and C4 (mimicked column with rebar in cone (quenching)). The heat-dissipating nature was observed, and the structural aspects were tested aftermath. The results reveal that the quenched specimen depicts better heat dissipation than the other specimens and eventually maintains the stability of the specimen throughout the height.

Keywords: biomimicry; cactus; damping ratio; dynamic analysis; heat dissipation; quenching

check for updates

Citation: Vishal, M.; Satyanarayanan, K.S. Experimental Investigation on the Heat Dissipation and Postfire Structural Performance of a Reinforced Concrete Column with Biomimicked Geometry. *Fire* **2022**, *5*, 205. https://doi.org/10.3390/fire5060205

Academic Editor: Tiago Miguel Ferreira

Received: 26 October 2022
Accepted: 26 November 2022
Published: 30 November 2022

1. Introduction

Living creatures function within a set of operational parameters that have evolved over the last 3.8 billion years. The name "biomimicry" comes from the Greek term "bios" and "mimicry", which mean "life" and "imitation", respectively. The art of mimicking nature shall be termed biomimicry. It entails studying natural items and copying their design to solve problems that humans meet in practice. The goal of biomimicry is not to replicate a natural shape, process, or ecosystem exactly; rather, it is used to draw design principles from biology and utilize them as a stimulus to generate unique products and ideas. Biomimicry may be used to tackle technological and social issues of any size. Designs derived from biomimicry may result in more sustainable solutions. Biomimicry is regarded as crucial for overcoming today's challenges, since the globe faces fast climate change and environmental deterioration. The ecosystem and nature may be emulated and contribute to a resilient, sustainable, and adaptively constructed environment, which increases natural environment regeneration and adaptability to climate change.

To create advanced engineered materials, innovative design methodologies are necessary [1]. Nature is a great source of inspiration for new design approaches. Plants and animals are frequently included in species, allowing engineers and scientists to investigate their structural patterns, material composition, and performance under extreme conditions. Bioinspired materials and structures have the potential to make our buildings more environmentally friendly, energy efficient, long-lasting, and durable. So far, there have been limited reviews of the use of bioinspired materials in this area. Several initiatives have been made; however, their study did not address large-scale applications for building scale structures [2].

Recent research indicates that employing a biomimetic method to generate innovative engineered materials with improved mechanical characteristics is becoming increasingly common. Depending on the type of application, natural-inspired building materials are available in a variety of forms. Using biomimicry in buildings will improve the net sustainability of the operation. To accomplish this, Oguntona et al. identified three critical factors—technology innovation, environmentally friendly legislation, and education—to label sustainability and energy management [3]. The architects were drawn to construct large-scale structures influenced by nature, perhaps due to the prevalent opinion that nature possesses superior and appealing shapes [4]. One such construction was inspired by termite mounds, which are abundant in hot and humid parts of Africa [5]. To safeguard the inner residents, a true scale termite mound has a natural ventilation system. In a termite mound, several inner chambers are linked to the exterior by capillary tunnels. Through the capillaries, colder air enters the termite mound, and heated air exits through the higher chambers.

Biomimicry has also been used in structural systems and philosophies. Grigorian created a theoretical framework for analyzing tree-based frame architectures [6]. Traditional theoretical methodologies, according to the study, could not explain the design concepts applied in natural structures. However, in natural structures such as trees, performance control (PC) solutions can handle the loading history. Yiatros et al. presented load-bearing ducts as a structural design strategy for enabling natural ventilation in a multistory office building. The spiral grain of a tree trunk was also addressed in the study to envision a helical structural system [7]. The final structure design incorporated a circular pattern with spiral bracing through the elevation, which provided some structural support.

Soltan et al. investigated a nacre-inspired concrete composite material with greater tensile and flexural strength than traditional concrete designs [8,9]. They also investigated several design techniques based on nacre's characteristics and discovered that multilayered concrete structures outperformed monolithic constructions. Furthermore, their design plans proposed the use of polyurethane glue and polymer wire mesh between concrete layers to simulate the interlayer properties of nacre. Sindhu Nachiar et al. studied the behavior of a pin jointed plane truss by biomimicking the humerus bone as a tension member and the femur bone as a compression member [10–13]. Musab Sabah Abed et al. created a knotted thin reinforced concrete column from on bamboo culm biomimicry, and the results showed that the constructed biomimicked design improved structural performance [14].

Aside from thorough structural design and analysis, biomimicry has inspired the unique design of additional features, such as a seismic load damper. Vibration dissipation devices are required for building buildings in active seismic zones. Kaluvan et al. created a bioinspired damping device that mimics the tendrils of a climber plant [15]. The helical spring system is based on a voided helical construction that employs magneto-rheological (MR) fluid. Under seismic stresses, various damping forces are obtained from altering the liquid potency inside the coil.

Plants and woods have flexible systems to defend themselves from the dry humid climate [16]. Reichert et al. created a self-governed architectural system which adapts to alterations in the environment. The study used natural behavior to imitate the hygroscopic qualities of wood veneer. In a field test, the study demonstrated an actual size construction of their suggested building wrapping system [17].

Many researchers have been concerned about the fire performance of reinforced concrete columns through various approaches [18–22]. Panwei Du et al. studied the behavior of hybrid fiber-reinforced high performance concrete columns under fire [23]. The test was performed under various load eccentricity conditions, and their structural behavior was observed. The results reveal that as load eccentricity increases, so does mid-height deflection and axial contraction. Zongping Chen et al. evaluated the eccentric compression performance of a reinforced recycled aggregate column at extreme temperatures [24]. The results indicate that the collapse mechanism of the eccentric columns shifted from tension to compression when the temperature or eccentricity ratio rose, whereas the RCA replacement percentage had a minimal effect.

Thomas Gernay proposed a new measure to supplement the fire resistance rating that reflects the unique impacts of the cooling phase and clearly describes the capacity of a structural element to withstand burnout [25]. Tan and Yao established an elementary and reasonable approach for predicting the resistance of fire in RC columns exposed to four-face heating by taking into account both uniaxial and biaxial column bending [26]. The findings demonstrate that the prediction model can directly anticipate the ultimate load and deflection of RC columns at elevated temperatures. To determine the resistance of fire in reinforced concrete columns, Shujaat H. Buch and Umesh K. Sharma created a model that took into account a number of important factors, such as the influence of premature concrete spalling during a fire, the impact of local longitudinal reinforcement buckling caused by explosive spalling, and the significance of reinforcement configuration [27–29].

Bajc et al. explored the resistance of fire in reinforced concrete columns under the impact of spalling and discovered that spalling can diminish the final fire resistance by up to 70% [30]. Rohola Rahnavard et al. conducted an experimental investigation into the resistance of fire in infilled concrete cold-formed steel built-up composite built-up columns and discovered that prognoses based on the simplified design method are highly conservative; however, prognoses based on standard methodologies are slightly cautious, necessitating further changes to increase accuracy [31,32].

Abdelkader Bougara and Abdelkadir Fellouh investigated how the eccentric loading, slenderness, reinforcement, rating of fire, and fire situation affected the fire performance of a partially-enclosed concrete column [33]. Zhiwei Shao et al. created a fire-resistant design approach for reinforced infilled concrete steel tube columns under compression [34]. They discovered that the suggested approach properly accounts for material strength dispersion to assure the durability of components at high temperatures. Weiyi Kong et al. studied the load transfer mechanism in reinforced concrete beam-column joints under fire exposure [35]. The results reveal that under symmetrical firing conditions, the total deformation mode of the beam-supporting column transfer structure is symmetrical about the structure's central axis. The transfer girder and upper beam segments rose to varied degrees of deflection.

Improvements in the fire resistance of columns and frames provide a significant contribution to the overall durability of the structure under fire [36–41]. Most of the conventional fire protection and resistance techniques involve adding another material, which eventually increases the cost. As a result, this work experimentally analyses the nature of heat dissipation through biomimetic geometry over a reinforced concrete column. The crucial novelty of this research is applying the heat dissipation nature of a cactus plant to a reinforced concrete column. This eventually protects the column by dissipating the heat through the altered geometry at the top, made from the same concrete material.

From previous research, it was found that plants with sharp pointed edges delineate better heat dissipation characteristics on hot days [42,43]. This concept was mimicked into a load-carrying structural member that could help under fire scenarios. Few geometries were taken, and their heat dissipation nature was observed. The best heat-dissipating geometry was considered for the experimental verification. Five column specimens with various conditions were heated to check the heat dissipation nature, and their post-fire structural performance was observed.

Application of the Proposed Concept in Prototype Buildings

The suggested concept can be incorporated into any structure during or after construction. The shape will be affixed to the top of the column that stretched above the roof. The installation of the shape will never have an effect on the structural performance of the column's superstructure region. Figure 1 explains the concept using an example of a conventional three-bay, two-story structure.

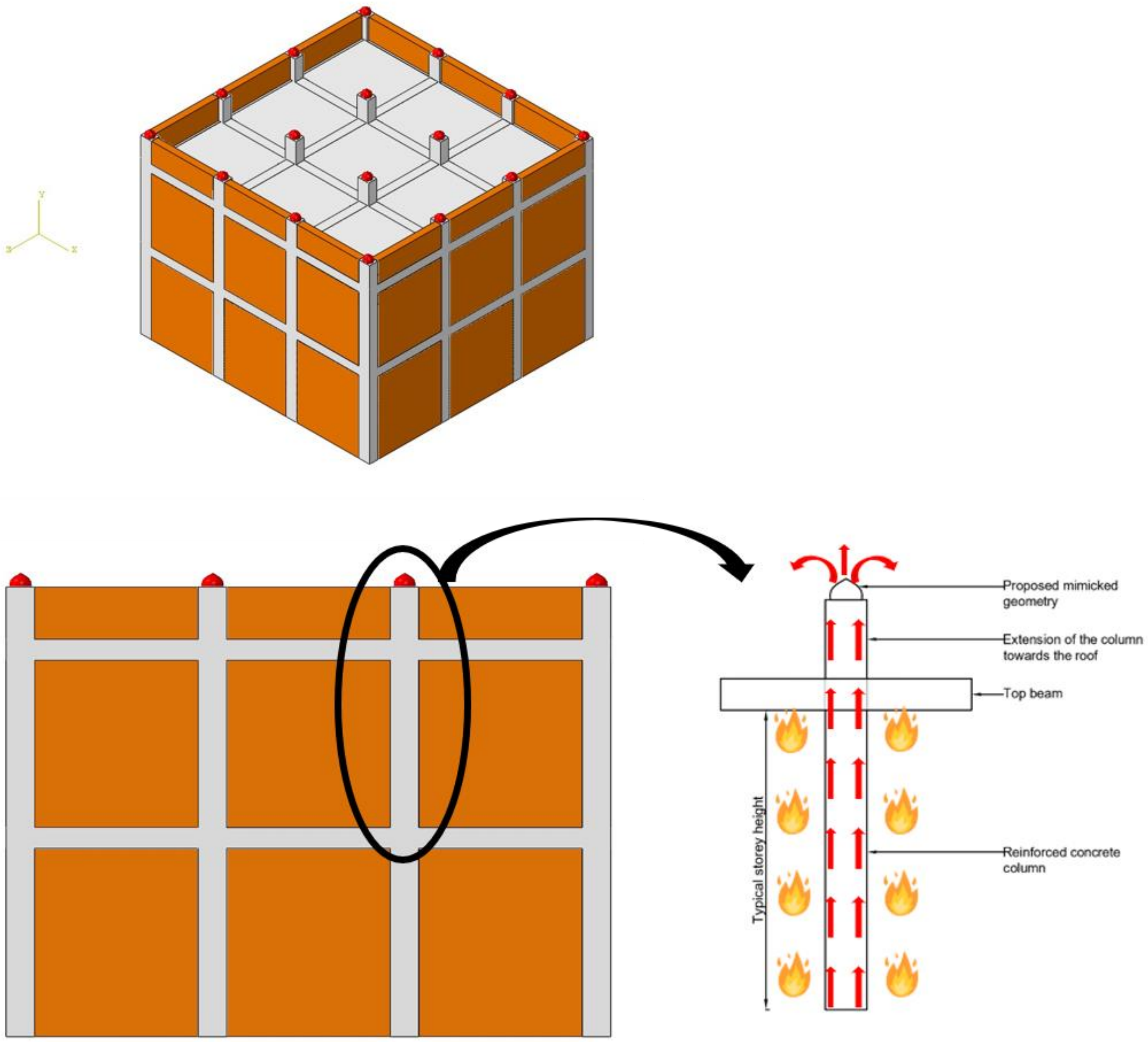

Figure 1. Representation of a biomimicked concept over the reinforced concrete column in a typical prototype building.

Through the biomimicked shape, heat will be transferred to the column's top in biomimetic columns. Whenever there is a fire in the structure, this shape naturally disperses the heat. In typical columns, heat accumulates in the column section, resulting in increased thermal damage. Figure 2 depicts the standard column under a fire scenario.

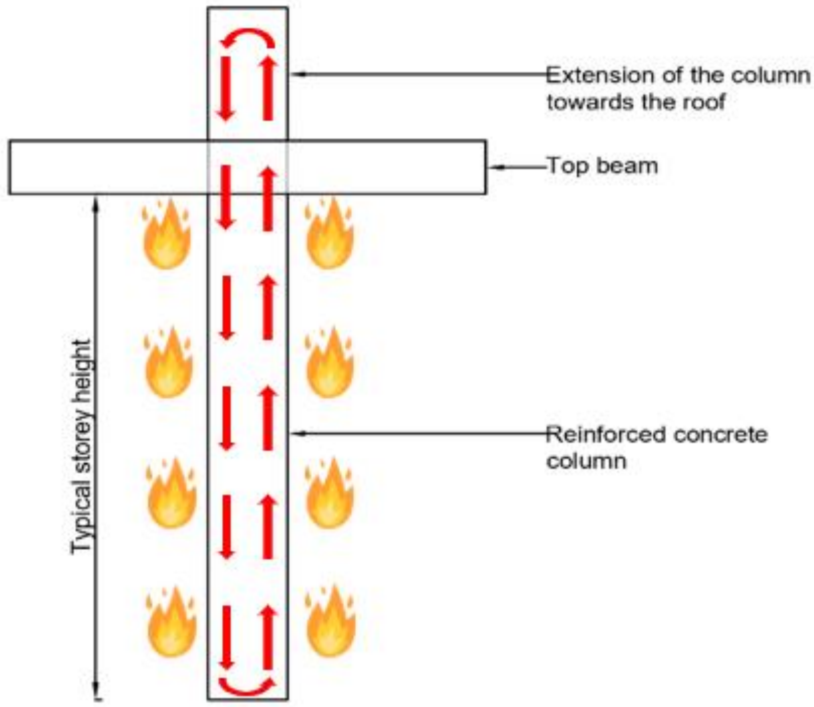

Figure 2. Conventional column under fire scenario.

The suggested design will effectively avoid fire damage to reinforced concrete columns in single and double-story structures.

2. Materials, Methods, and Experiments

The methodology of the entire study is summarized in a flow chart and represented in Figure 3.

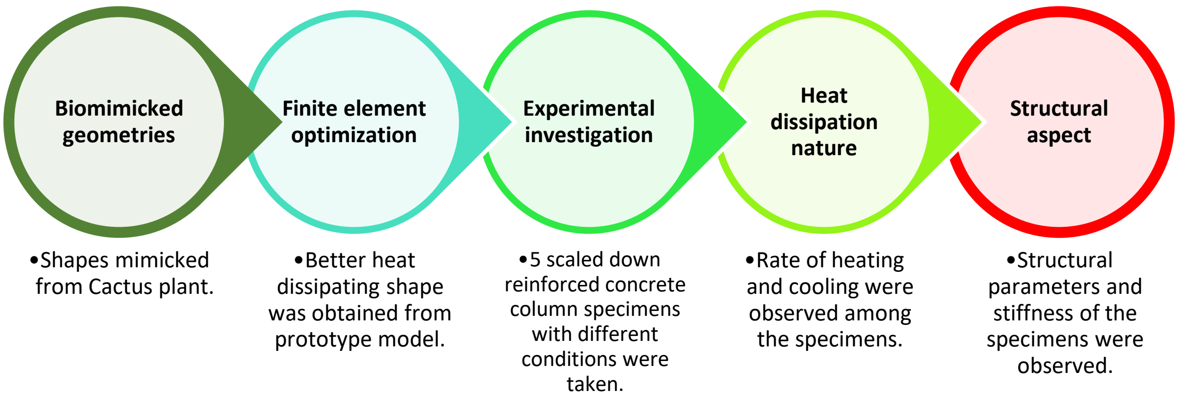

Figure 3. Methodology of the study.

Few sharp pointed shapes were taken into account based on the Saguaro Cactus [44]. The shape was optimized using finite element analysis through a prototype model. The visual comparison of a Saguaro Cactus and the proposed mimicked shape is represented in Figure 4. The various shapes adopted for the optimization are represented in Figure 5.

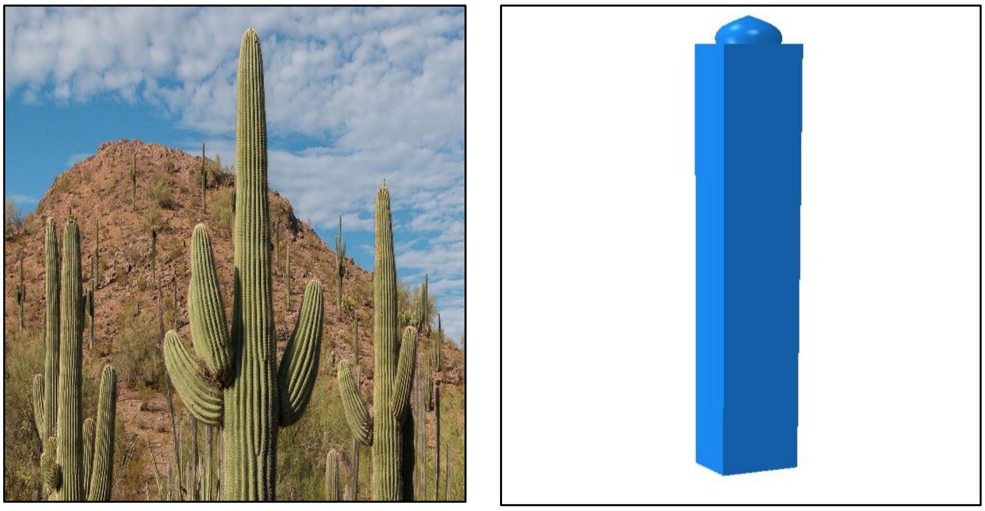

(a) (b)

Figure 4. (**a**) Saguaro Cactus plant. (**b**) Proposed mimicked shape in column.

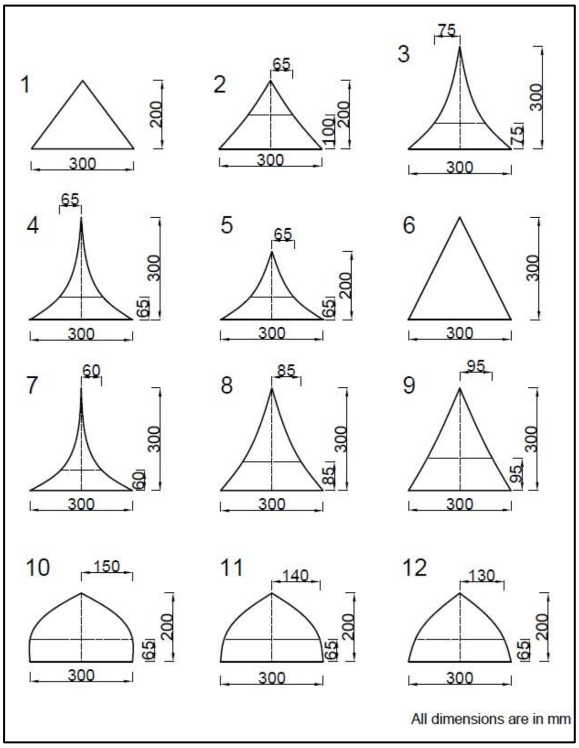

Figure 5. Various geometries adopted for optimization based on the cactus plant.

The prototype model was designed as per IS 456:2000 [45] and has a cross-section of 300 × 400 mm for a height of 3000 mm. For reinforcements, 4 numbers of 16 mm diameter bars were provided as main reinforcements, and 8 mm lateral ties were provided at a spacing of 200 mm C/C. Transient heat analysis was performed using the finite element software ABAQUS v6.14. The concrete section was modeled as a 3-D deformable element, and reinforcements were modeled as wire elements [46–48]. M30 grade of concrete with a damaged plasticity model and Fe500 grade of steel was taken for the finite element analysis [49]. The material properties for the finite element studies were taken from a previous study and EN 1992-1-2 [50]. The connection between the concrete and steel was considered an embedded connection.

This study was performed by applying heat without any load over the section. The self-weight of the section was considered, and surface heat flux was applied with desired magnitude all over the four longitudinal faces of the column, similar to the real-time situation. A typical heat transfer problem consists of conduction, convection, and radiation, as stated in Equations (1) and (2) [23].

$$\rho c \frac{\partial T}{\partial t} = \frac{\partial}{\partial x}\left(k \frac{\partial T}{\partial x}\right) + \frac{\partial}{\partial y}\left(\frac{\partial T}{\partial y}\right) T \tag{1}$$

$$-\left(k \frac{\partial T}{\partial T} + k \frac{\partial T}{\partial T}\right) = h_0 \left(T_f - T_0\right) + \varepsilon_0 \left(T_f^4 - T_0^4\right) \tag{2}$$

where ρ is the concrete's density, k is the thermal conductivity, c is the specific heat, h_0 is the convection coefficient, which equals 25 W/m^2K, T_f is the temperature of the fire curve, T_0 is the temperature at the concrete surface, σ is the Stefan–Boltzmann constant, and ε_0 is the concrete surface emissivity (0.7) [23].

The best heat-dissipating shape was considered, and it was tested experimentally. For experimental validation, five column specimens with different conditions were considered in this study. The specimens were named C (conventional nonheated column), C1 (conventional heated column), C2 (mimicked column), C3 (mimicked column with rebar in cone), and C4 (mimicked column with rebar in cone (quenching). After 28 days, the concrete had an average cube strength of 31.4 N/mm^2. Crushed stone aggregates with a maximum size of 10 mm were utilized as coarse aggregates, while river sand was used as fine aggregates at a water to cement ratio of 0.45. For rebar, Fe 500 grade of steel with an average yield stress of 546.83 N/mm^2 and an average ultimate stress of 623.78 N/mm^2 was employed.

The schematic flow of the entire experimental procedure is given in Figure 6. Heat was applied to the specimens using an indigenous high-temperature localized heating element, as shown in Figure 7. It has a capacity to heat up to 1200 °C, and the heating profile was based on ISO 834 standard fire curve [51]. The heating element could accommodate a cross-section of 125 × 125 mm for a span of 600 mm.

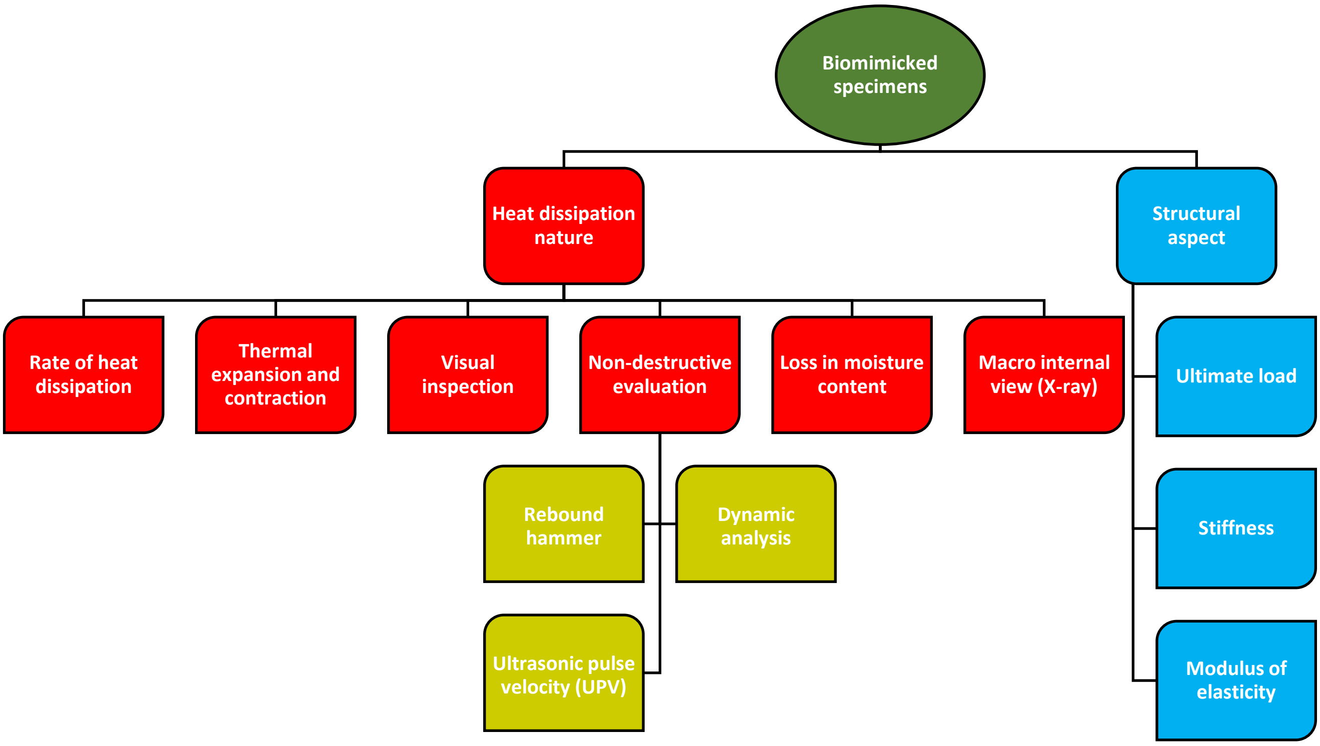

Figure 6. The schematic flow of the entire experimental procedure.

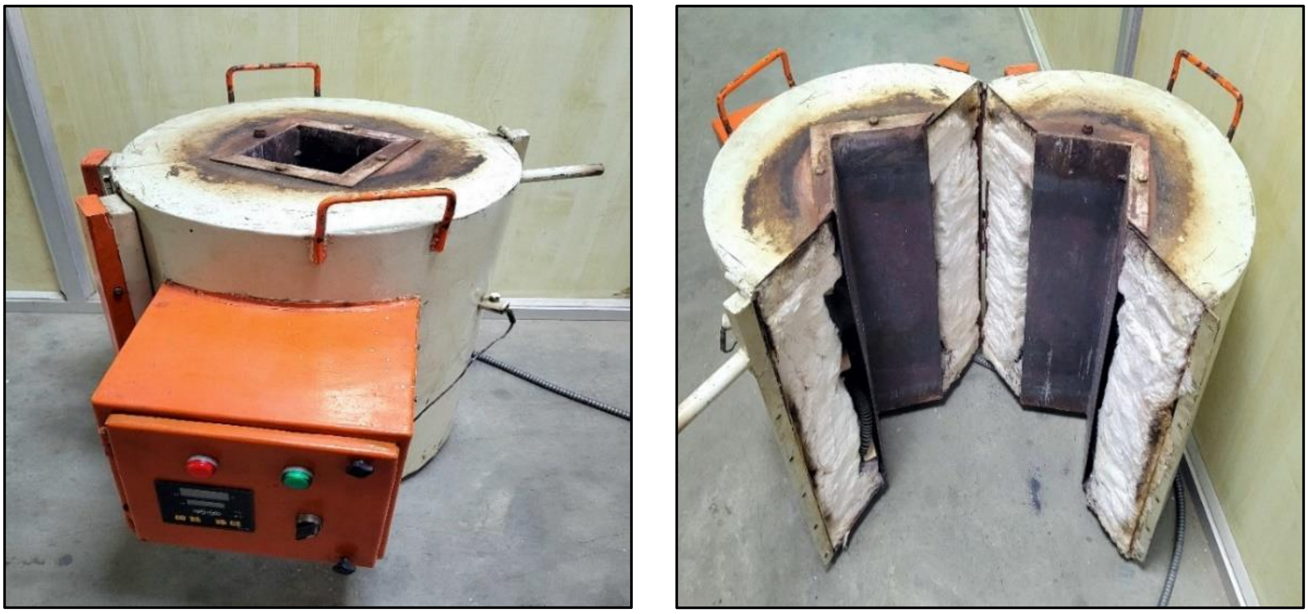

(**a**) (**b**)

Figure 7. High-temperature localized heating element. (**a**) Overall view. (**b**) Open view.

The weight of the column specimens was recorded before and after heating the specimens. Similarly, a nondestructive test was performed before and after heating the specimens to check the changes in the internal characteristics. The natural frequency was measured through ambient vibration measurements for the fire-affected columns to identify the changes that occurred in the dynamic nature of the specimens after fire exposure. After that, the ultimate load capacity of the column specimens was identified by applying axial load to the specimens, and structural parameters were observed.

3. Optimization through Finite Element Analysis

Transient analysis was performed for the conventional column and columns with 12 different geometries, and the inner core temperature was recorded with respect to the height. The comparison of the core temperatures with respect to the height for the columns with different shapes is represented in Figure 8. From the figure, it is clear that the shape has a significant effect over the top region of the columns. When compared to the conventional column, all the shapes exhibit good heat-dissipating signatures up to 1000 mm from the top. This shows that the top of the column region could be easily saved in the fire scenario. The mimicked column with cone 10 shows excellent heat release characteristics compared to all other shapes. This shows the effect of geometry in terms of heat release behavior.

For better representation, the heat dissipation of the column specimen with cone 10 and the conventional column was compared and is shown in Figure 9. At the top of the column, the temperature of the conventional column was 752 °C, and the column specimen with cone 10 was 655 °C. The temperature of the column specimen with cone 10 tends to be 14.8% less than the temperature of the conventional column at the top. This heat dissipation works similarly to the fire protection technique. Implementing a simple shape could prevent the collapse of the column. A pictorial representation of the heat release contours of the conventional column and mimicked column with cone 10 is shown in Figure 10.

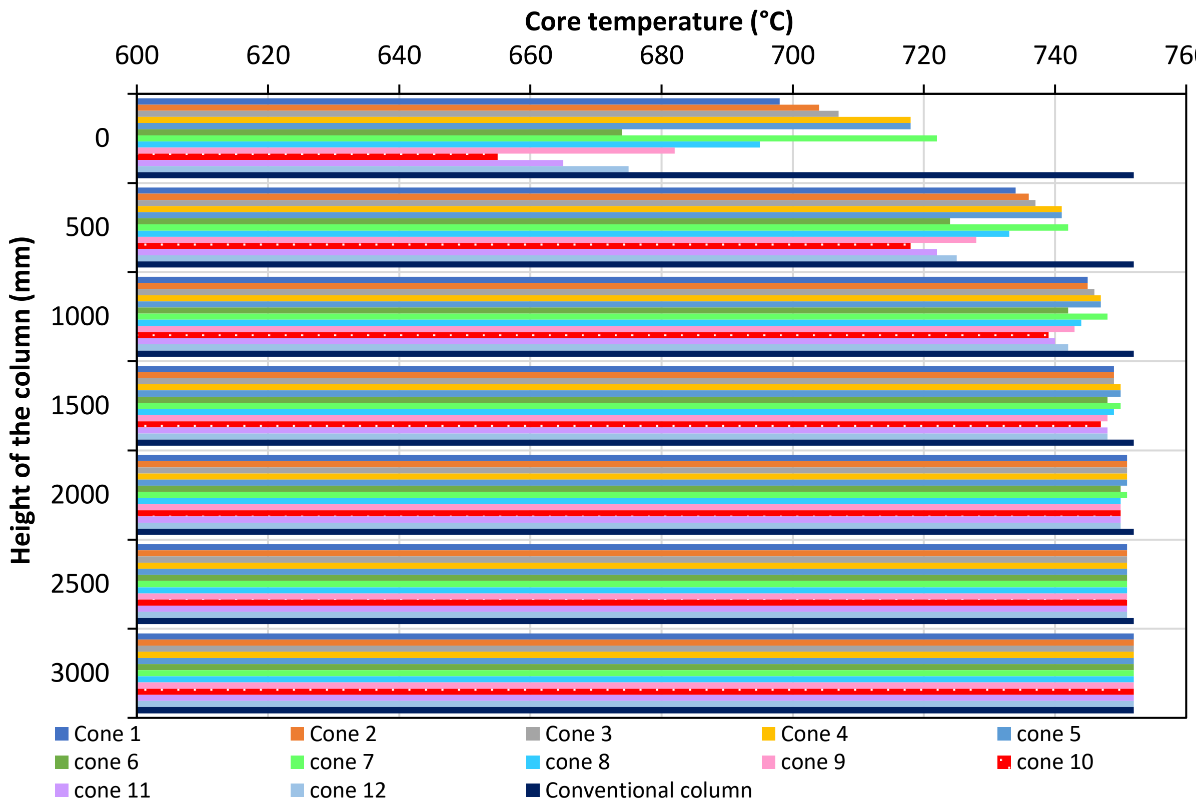

Figure 8. Comparison of the core temperatures with respect to height for the columns.

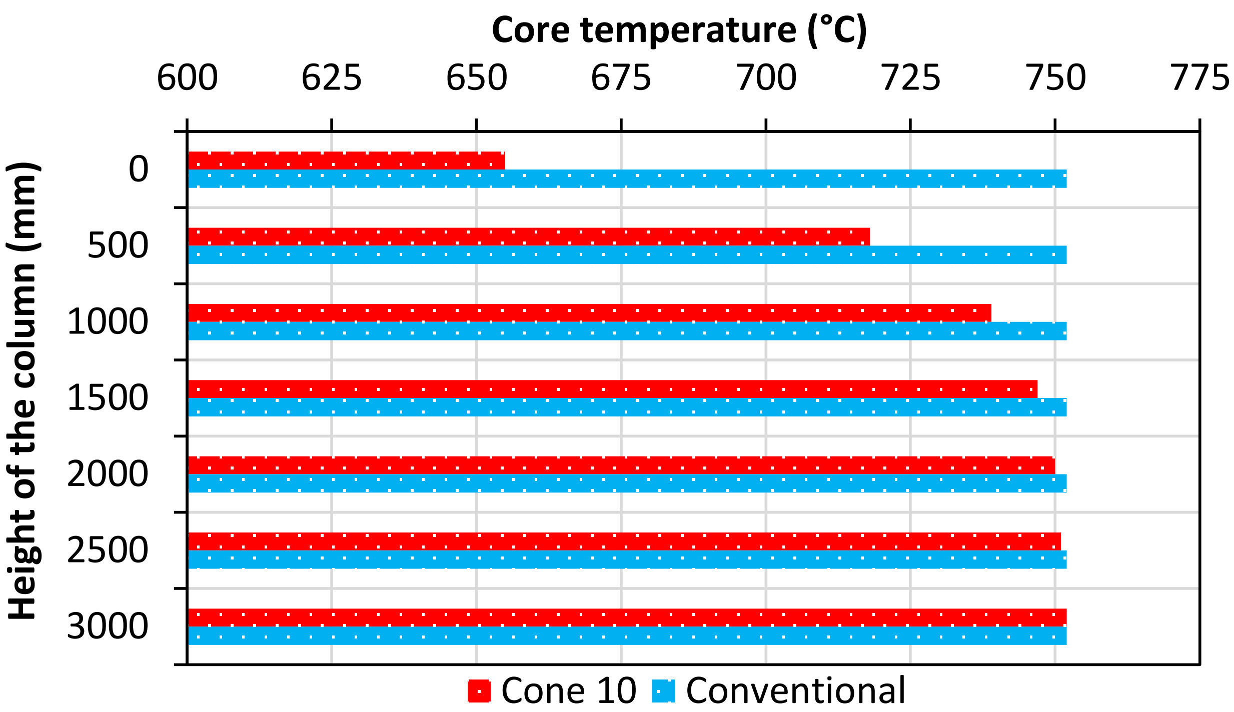

Figure 9. Heat dissipation of the column specimen with cone 10 and the conventional column.

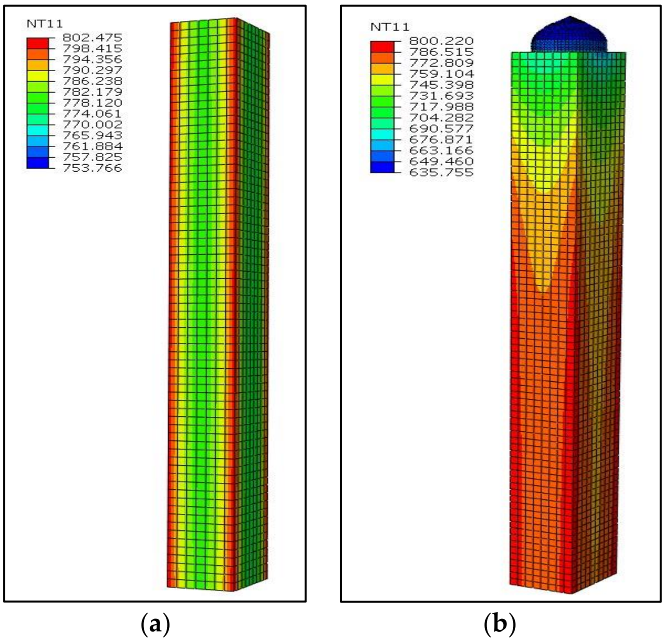

Figure 10. (**a**) Heat release contours of the conventional column and (**b**) heat release contours of the mimicked column with cone 10.

4. Experimental Setup

A scaled-down model of a reinforced concrete column was considered to validate the effect of heat dissipation in the mimicked column through experiments. For experimental purposes, the columns were scaled down to a ratio of 1:4 from the prototype model. The scaled-down model has a cross-section of 75×100 mm and a height of 750 mm. It comprises 4 numbers of 6 mm diameter bars as the main reinforcement and 6 mm lateral ties as a spacing of 50 mm C/C. For the mimicked shape, the mold was prepared using mild steel. A wooden mold was prepared for the columns. The mimicked part was attached to the wooden mold at the top through bolts. The dimensions of the scaled-down mimicked shape are given in Figure 11.

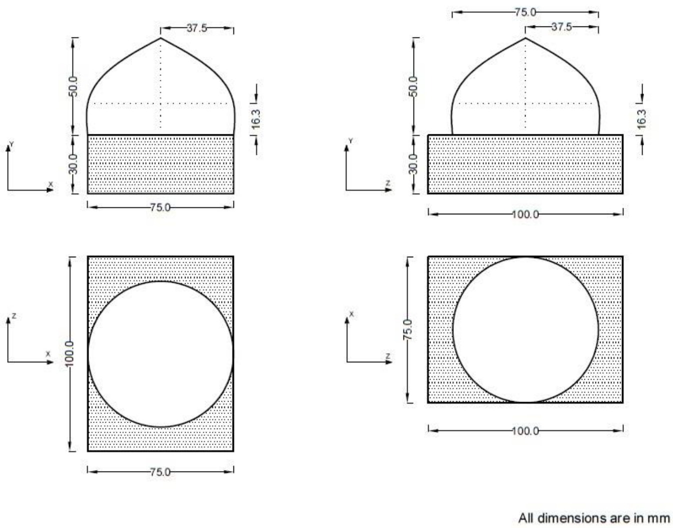

Figure 11. The dimensions of the scaled-down mimicked shape.

Based on the dimensions, the mold of the mimicked part was fabricated. The fabricated mimicked mold is represented in Figure 12.

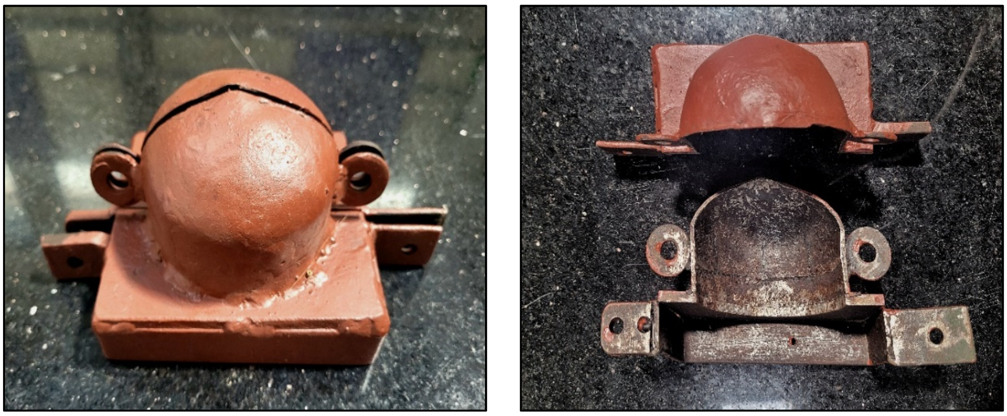

(**a**) (**b**)

Figure 12. Fabricated mimicked mold. (**a**) Overall view. (**b**) Open view.

Thermocouples were placed inside the reinforced concrete section to measure the core temperature while heating. The thermocouples were placed at the top, middle, and bottom core regions of the column. For the mimicked shape specimens, a thermocouple was placed at the top of the cone. A schematic representation of the placement of thermocouples for the conventional and mimicked columns is shown in Figure 13.

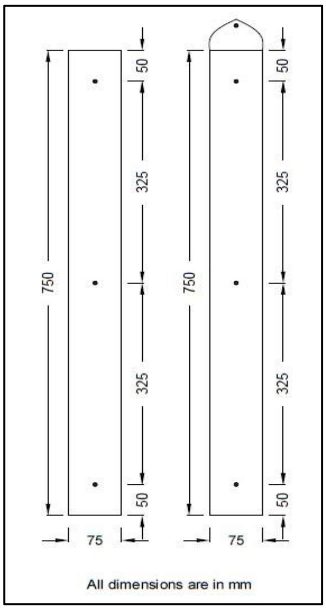

Figure 13. Placement of thermocouples for the conventional and mimicked columns.

The black dots represent the thermocouples that were placed inside the columns. The thermocouples were inserted through the fresh concrete after placing it. Holes were drilled in the wooden mold at a specified distance to insert the thermocouples. For columns C3 and C4, the main reinforcements were extended to the mimicked part, as shown in Figure 14a.

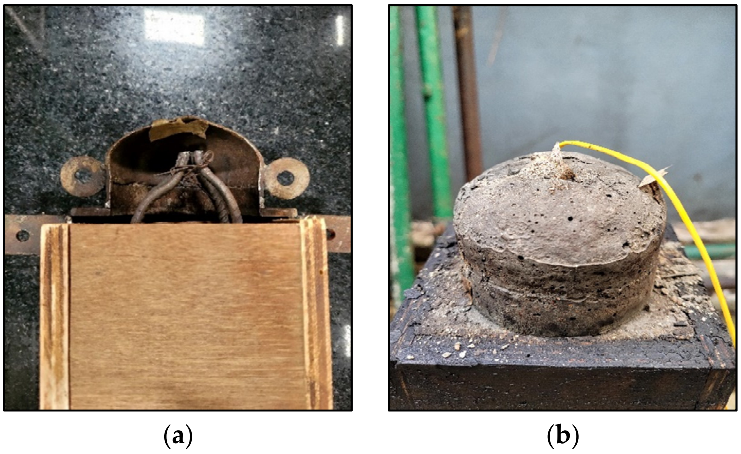

Figure 14. (a) Representation of the extension of the main reinforcement to the mimicked part. (b) Demolded image of the mimicked part.

The concrete was placed vertically into the mold and hand compaction was performed. After placing the concrete, the column was made to stand vertically along with a temporary support. The mimicked part was demolded, followed by the column part after 24 hours. Figure 14b represents the demolded image of the mimicked part after 24 hours. After demolding, the entire column was placed inside the water for curing. The curing process was followed for 28 days, after which the experiments were performed.

A schematic test setup for conventional and mimicked columns is represented in Figure 15. The setup was arranged in a column testing frame. The heating element was placed inside the column testing frame using a support bar. The specimen was inserted into the heating element from the top, and the specimen was placed over the dummy support. The specimen was placed inside the heating element in such a way that the sides of the specimen did not make any contact with the inner side of the heating element. The specimen was packed with glass wool near the top and bottom entry regions of the heating element to minimize the heat loss. All thermocouples were attached to the temperature indicator. An LVDT was set at the top to measure the expansion and contraction of the specimen under the influence of high temperature.

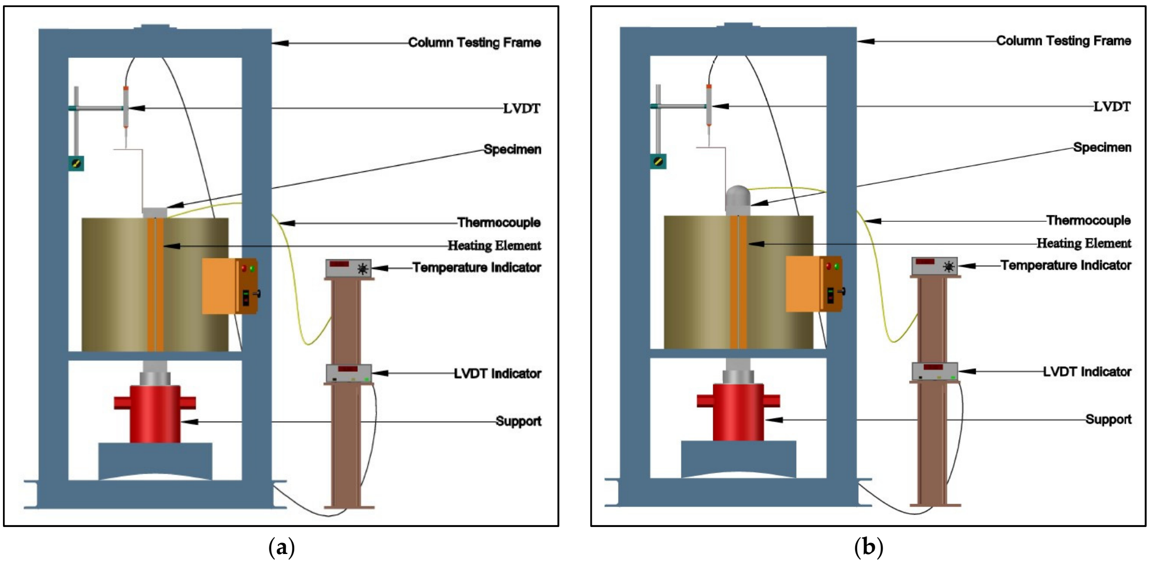

Figure 15. Schematic representation of test setup for (a) Conventional column. (b) Mimicked column.

A temperature of 250 °C was applied to the specimens for 4 hours. The main aim of the experiments was to check the influence of heat dissipation through the mimicked geometry and not to fail the specimen through high temperature. Therefore, the temperature was restricted to 250 °C, as it was considered to fall within the permissible temperature limit of the concrete. A total of 12 hours of observation was recorded, which included 4 hours of heating and 8 hours of temperature reduction. The temperature was applied through the heating element, which was predetermined to reach the desired temperature with correspondence to the ISO 834 standard fire curve. Figure 16 represents the similitude between the rise in an oven temperature and the ISO 834 standard fire curve up to 250 °C.

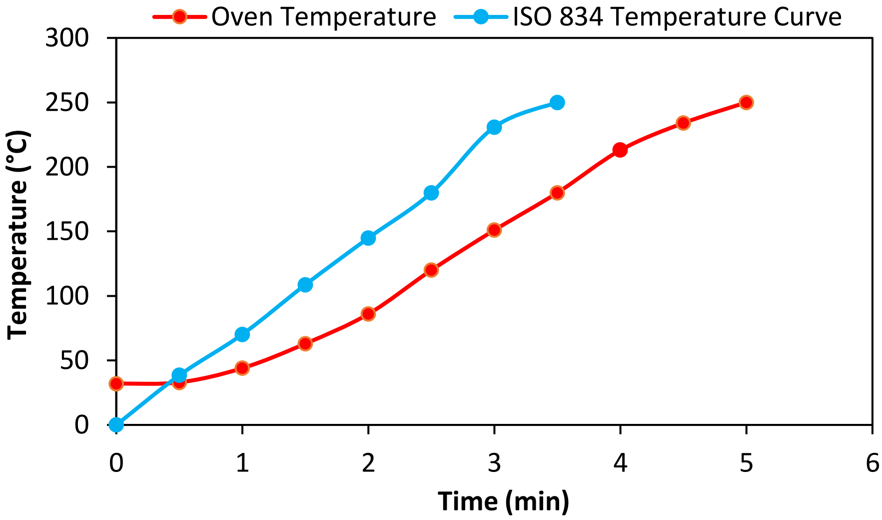

Figure 16. Comparison of the rise in an oven temperature and ISO 834 standard fire curve up to 250 °C.

5. Results and Discussion

5.1. Initial Observation

The room temperature and relative humidity were measured while testing each specimen. The initial temperature was also recorded before initiating the heating element. The room temperature, humidity, and initial temperatures in the top, middle, and bottom regions of the specimens are given in Table 1.

Table 1. Room temperature, humidity and initial temperatures in the top, middle, and bottom regions of the specimens.

	Room Temperature (°C)	Humidity (%)	Temperature in Cone (°C)	Temperature in Top (°C)	Temperature in Middle (°C)	Temperature in Bottom (°C)
C1	31	69	-	30	30	30
C2	29	71	29	31	33	32
C3	39	66	40	34	36	35
C4	39	90	41	41	43	42

The temperature and LVDT readings were recorded every 2 minutes. The heating efficiency of the heating element may vary based on external factors. In this regard, the maximum temperature reached in the top, middle, bottom, and mimicked cone regions was observed with correspondence to time. The observed data are presented in Table 2.

Table 2. Maximum temperature reached in the top, middle, bottom, and mimicked cone regions with respect to time.

Specimen	Maximum Temperature Reached with Respect to Time			
	Cone	**Top**	**Middle**	**Bottom**
C1	-	108 °C at 280 min	238 °C at 250 min	78 °C at 280 min
C2	66 °C at 290 min	103 °C at 256 min	239 °C at 250 min	83 °C at 292 min
C3	73 °C at 312 min	106 °C at 264 min	230 °C at 254 min	69 °C at 248 min
C4	64 °C at 190 min	84 °C at 212 min	245 °C at 256 min	87 °C at 228 min

The maximum temperature was reached in the middle region as the heat generated by the heating element was high in the middle region. The maximum temperature reached by the specimens in the regions was almost the same, but the time taken to reach the maximum temperature had some slight variation.

5.2. Time Versus Temperature Characteristics of the Specimens

Time versus temperature curves were plotted based on the temperature recorded in the top, middle, bottom, and mimicked cone parts, and are represented in Figure 17.

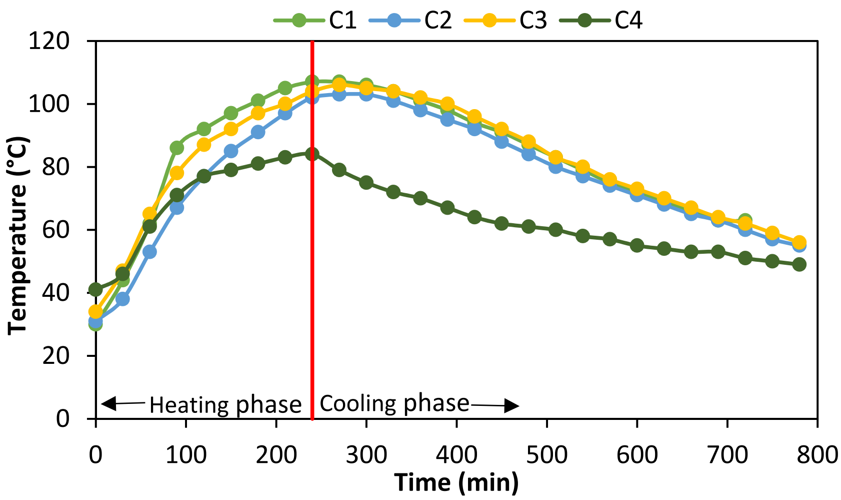

(**a**)

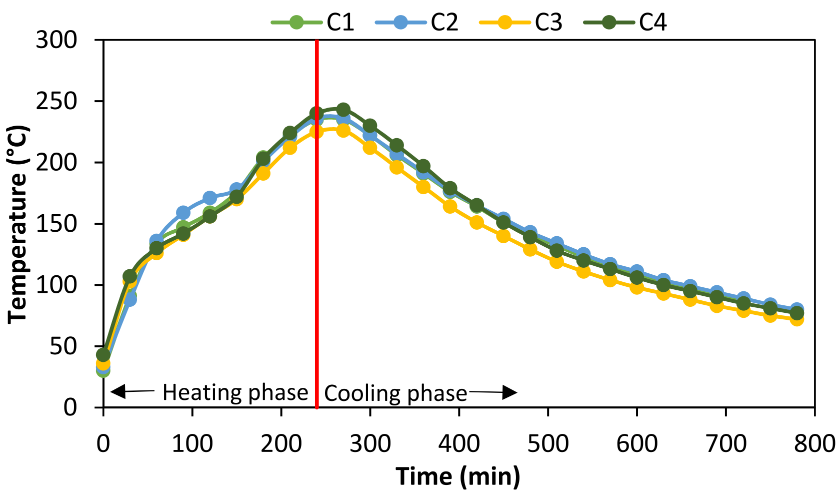

(**b**)

Figure 17. *Cont.*

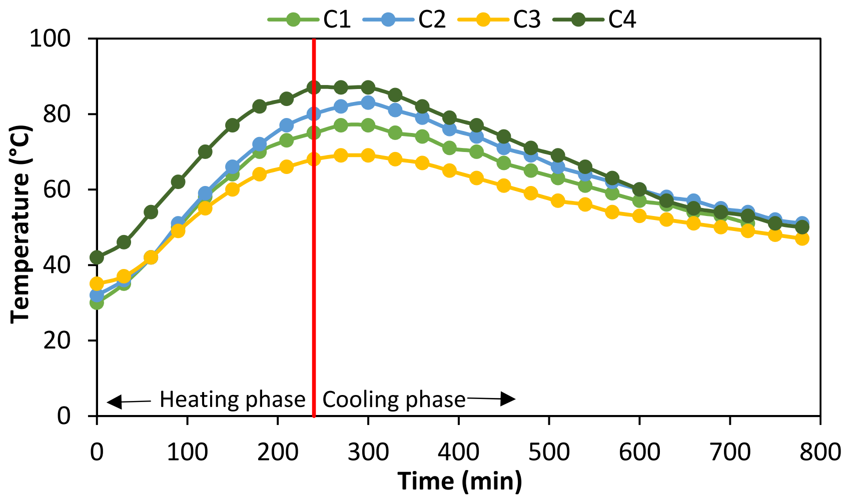

(**c**)

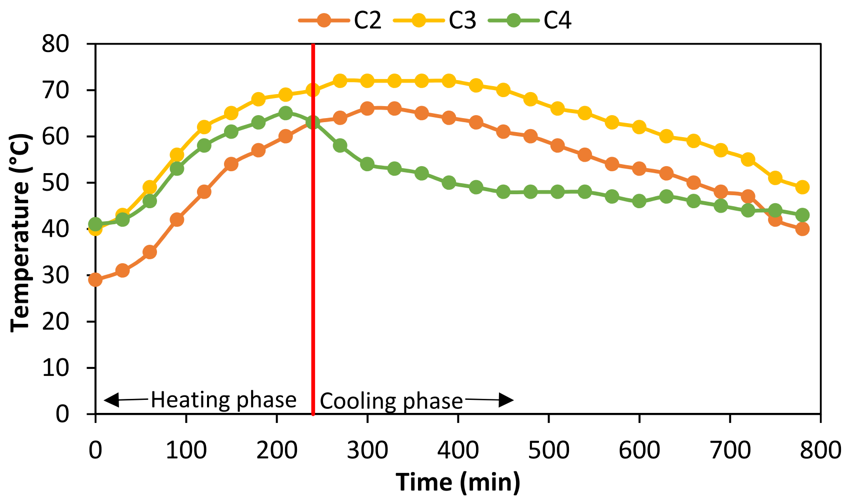

(**d**)

Figure 17. Time versus temperature curves for the regions at (**a**) top, (**b**) middle, (**c**) and bottom (**d**) mimicked cone.

The time versus temperature curves exhibit similar characteristics between the specimens throughout the heating phase. C4 has a slight drop in the temperature over the mimicked cone part and in the top region as a result of quenching. The dissipation of heat in the top region was obvious as a result of quenching in the cone part. For better understanding, the rate of temperature rise per minute under heating and the rate of temperature fall per minute under the cooling phase are computed and represented in Figure 18. The rate of temperature per minute was calculated by the maximum temperature reached while heating or cooling, with respect to the corresponding time in minutes.

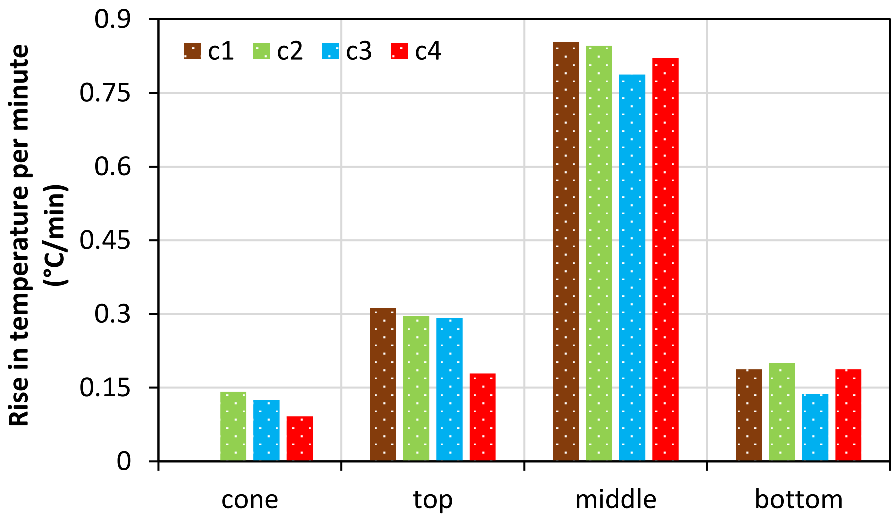

(**a**)

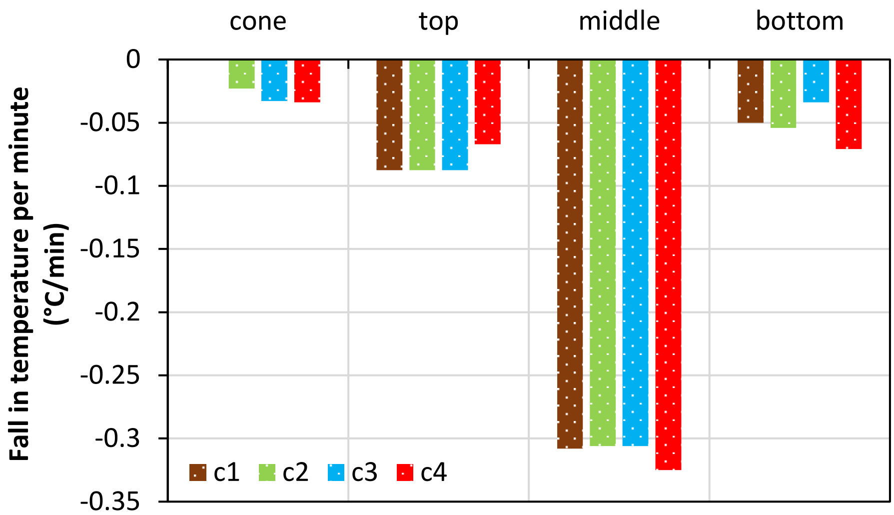

(**b**)

Figure 18. (**a**) The rate of temperature rise per minute under heating. (**b**) The rate of temperature fall per minute under the cooling phase.

A good heat-dissipating character shows a slower rise in temperature while heating and faster fall in temperature while cooling. While heating, it can be seen that the mimicked geometries have slower rising rates than specimen C1. While cooling, specimens C1, C2, and C3 follow almost similar rates except C4. The middle and bottom portions of C4 have higher rates than the top region when compared to other specimens. The heat accumulated in the middle and bottom regions was constantly released toward the top and resulted in a lower falling rate at the top. While cooling, the temperature at the top was almost constant for a longer duration. Meanwhile, there was a faster reduction in temperature in the middle and bottom regions. This shows the heat flow toward the top and the mimicked part trying to maintain the same temperature throughout the specimen. The temperature rise in the specimens at the top, middle, bottom, and cone regions every hour is represented in Figure 19.

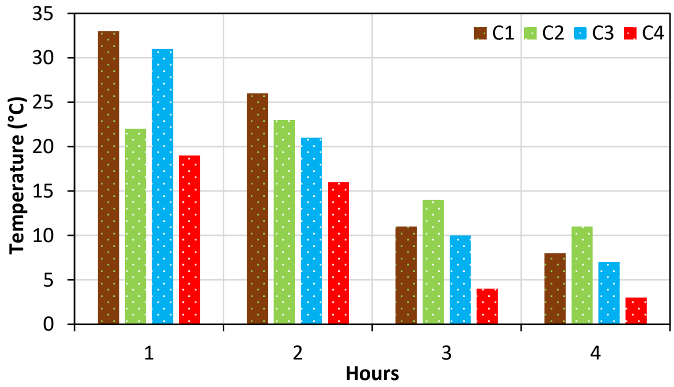

(**a**)

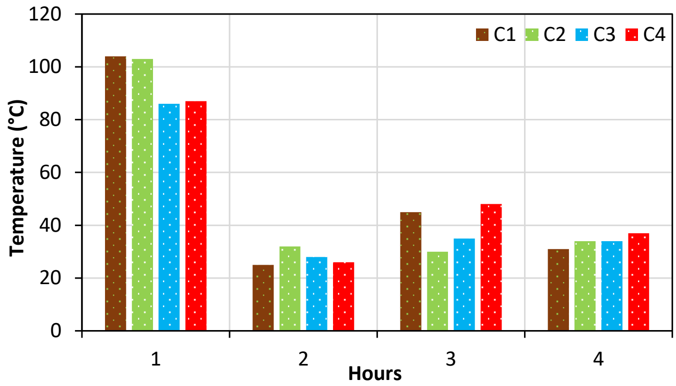

(**b**)

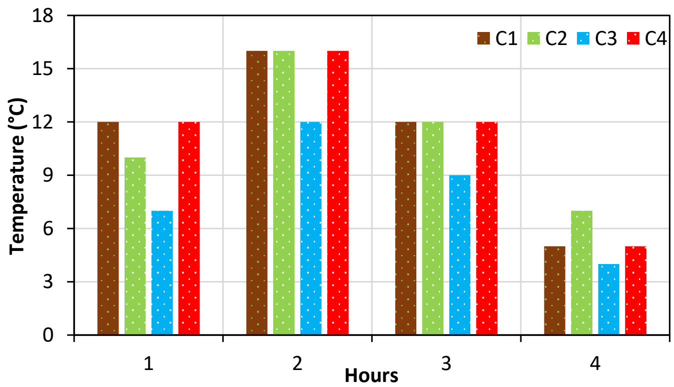

(**c**)

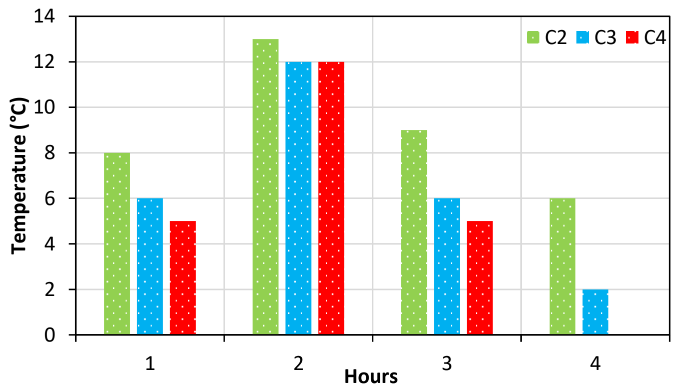

(**d**)

Figure 19. Temperature rise in the specimens every hour at (**a**) top, (**b**) middle, (**c**) and bottom (**d**) cone.

While heating, the temperature rise of specimens C3 and C4 in the top region was very low, but the temperature rise in the middle and bottom regions was greater than that of the other specimens. The opposite condition occurred for specimens C1 and C2 with respect to C3 and C4. Specimens C3 and C4 have rebar connected from the main reinforcements, which results in good dissipation of heat at the top region. Meanwhile, the middle region, which is heated the most, transfers the heat accumulated in the middle and bottom regions toward the top. This makes the top region stay at a specific temperature for a longer duration, neither increasing or dropping. The absence of cones or cones with rebar in specimen C1 does not allow the temperature to flow toward the top or other regions. C2 has a shape that has no rebar extended toward the cone and dissipates less than C3 and C4. In fact, the heat transfer is predominantly based on the conductivity of the material. Steel has better conductance than concrete, which helps specimens C3 and C4 dissipate more heat than C2, which has no rebar extended toward the cone. Hence, specimens C3 and C4 exhibit better heat dissipation than the other specimens. The temperature rise per hour in the cone region clearly depicts the effect of heat dissipation. The presence of extended rebar at the cone region does not allow the temperature to rise as it was maintained at a constant rate. The rate of temperature decreases every hour, while cooling in the top, middle, bottom, and cone regions for the specimens is represented in Figure 20.

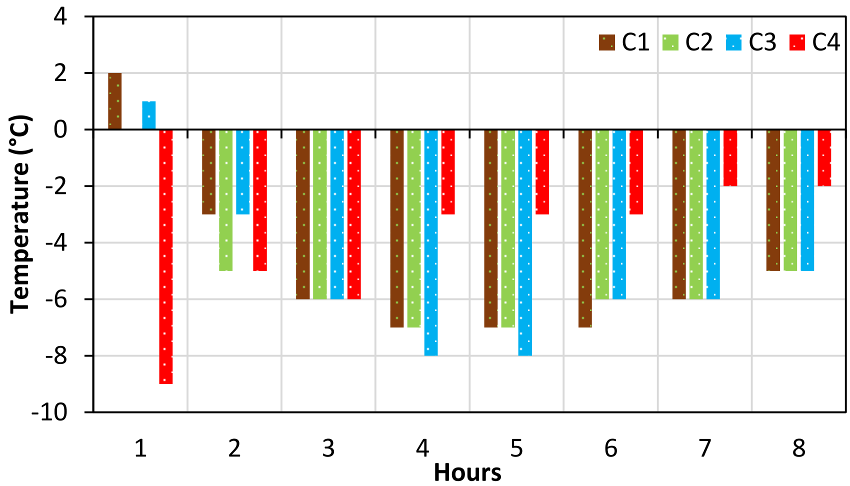

(**a**)

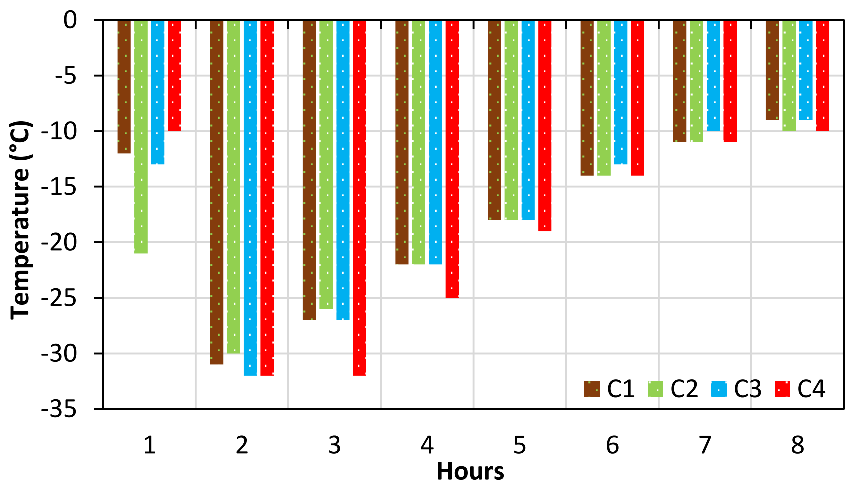

(**b**)

Figure 20. *Cont.*

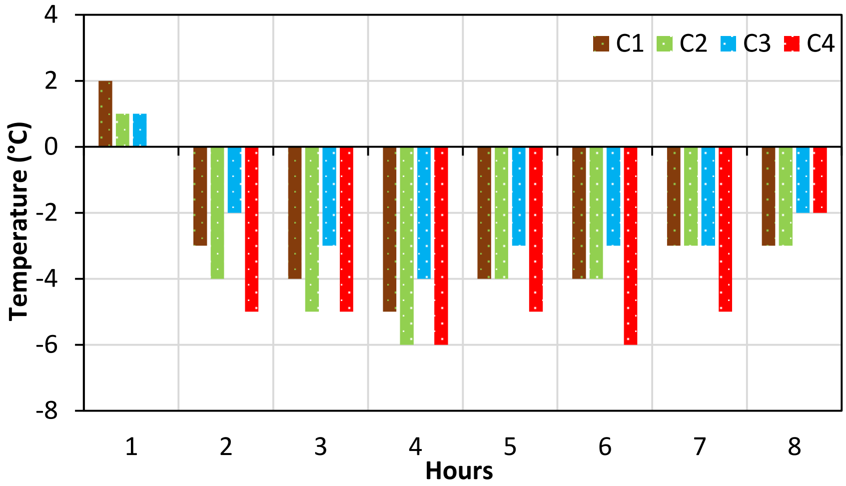

(**c**)

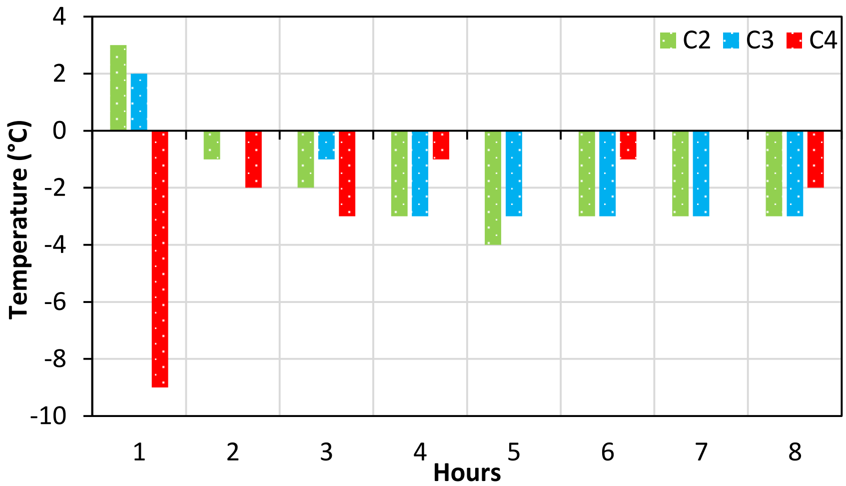

(**d**)

Figure 20. The rate of temperature fall in the specimens every hour at the (**a**) top, (**b**) middle, (**c**) bottom, and (**d**) cone.

While cooling, the quenched specimen C4 had faster and better heat release in all regions than the other specimens. Apart from C4, specimens C2 and C3 have better falling rates than C1 in the top and middle regions. The rate of falling was high for specimens C2 and C3 up to the initial 4 hours of cooling. Newton's Law of Cooling states that the rate of heat loss of a substance is exactly proportional to the temperature differential between the material and the environment. Equation represents Newton's Law of Cooling (3),

$$T(t) = T_s + (T_0 - T_s)e^{-kt} \tag{3}$$

where $T(t)$ is the temperature of the object at time 't', T_s is the surrounding temperature, T_0 is the initial temperature of the body, and k is a constant of proportionality.

The temperature contrast was high, so the rate of temperature fall was high during those stages. Once the temperature difference is smaller, the rate of temperature decreases dips and becomes similar to that of specimen C1.

5.3. Thermal Expansion and Contraction

The LVDT readings exhibit thermal expansion due to heat and contraction due to cooling. Whenever an element is subjected to high temperature, it will undergo expansion as a result of heat release. This heat release will produce thermal stresses, and these stresses will be released by forming cracks over the surface. Therefore, the maximum expanded element will undergo maximum contraction [52]. From the curves, it was clear that the most heat dissipated specimen was C4 as it underwent the maximum expansion and contraction. Specimen C1 underwent the least expansion and contraction, thus proving the lowest heat dissipation characteristics. Specimens C2 and C3 fall next to specimen C1 in terms of heat dissipation. The thermal expansion and contraction subjected to time are shown in Figure 21.

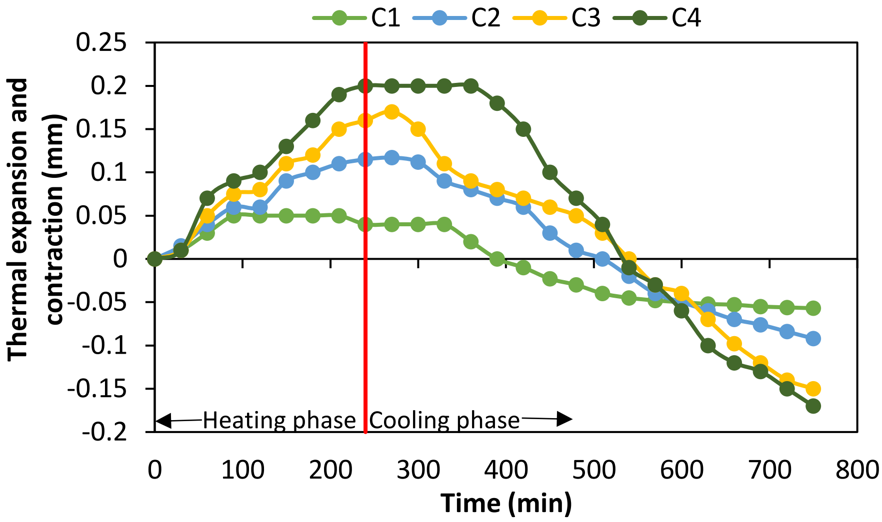

Figure 21. Thermal expansion and contraction of the specimens with respect to time.

5.4. Visual Inspection

After heating, visual inspection was performed to check the color changes and formation of cracks. Figure 22 represents the post fire images of the column specimens. No visual cracks were formed over specimen C1. More cracks were formed over specimen C4, followed by C3 and C2. The heat dissipation resulted in the emergence of surface cracks as a result of the release of thermal stresses. The most heat dissipated specimens C4 and C3 have a slight change in color rather than the specimens C2 and C1. Following visual inspection, nondestructive tests, namely ultrasonic pulse velocity and rebound hammer tests, were performed.

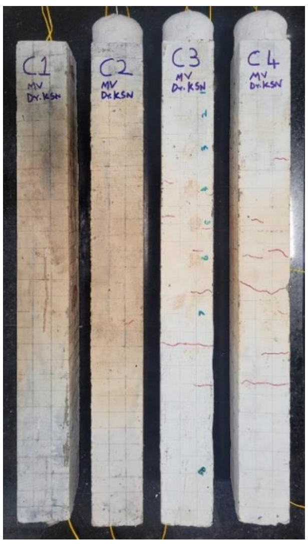

Figure 22. Postfire images of the specimens.

5.5. Nondestructive Evaluation

The UPV and rebound hammer tests were executed before and after heating the specimens in the top, middle, and bottom regions. The velocity and the rebound number for specimens have similar trends before and after the heating scenario. Specimens C1 and C2 have slight dips in velocity and rebound number after heating. Specimens C3 and C4 have massive curtailment after heating. Heat dissipation triggers the generation of cracks to release thermal stresses, which results in a reduction in strength. This shows that the formation of thermal cracks influences the strength of the section. The velocity calculated from the UPV and rebound number at the regions of the specimens are represented in Figures 23 and 24.

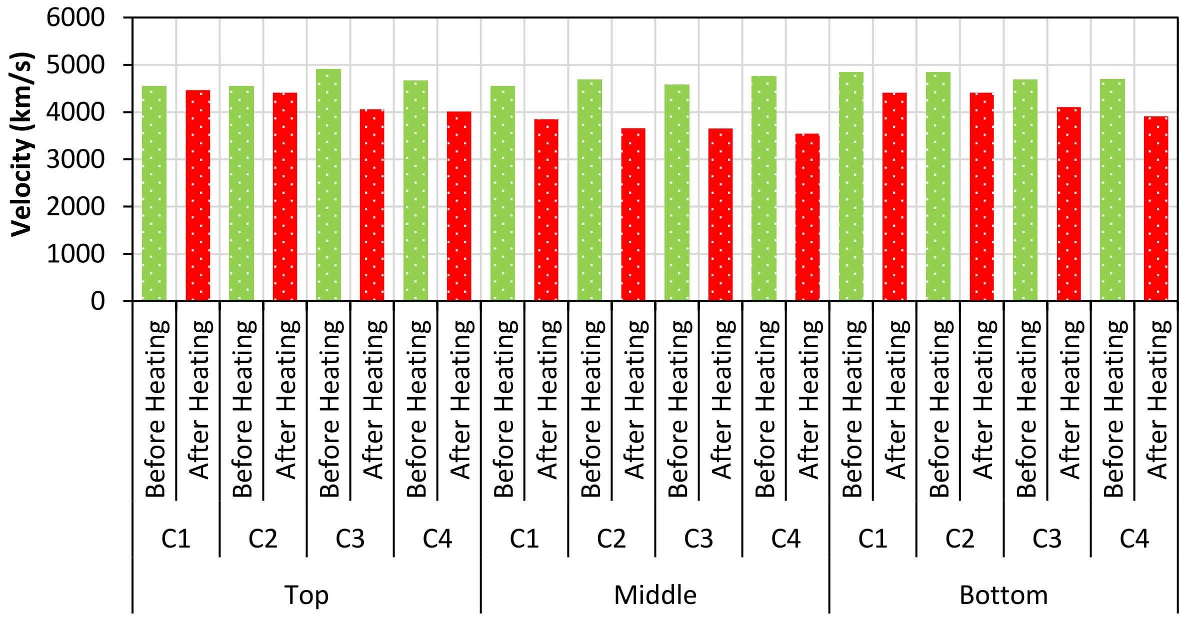

Figure 23. Observed velocity of the specimens at three regions.

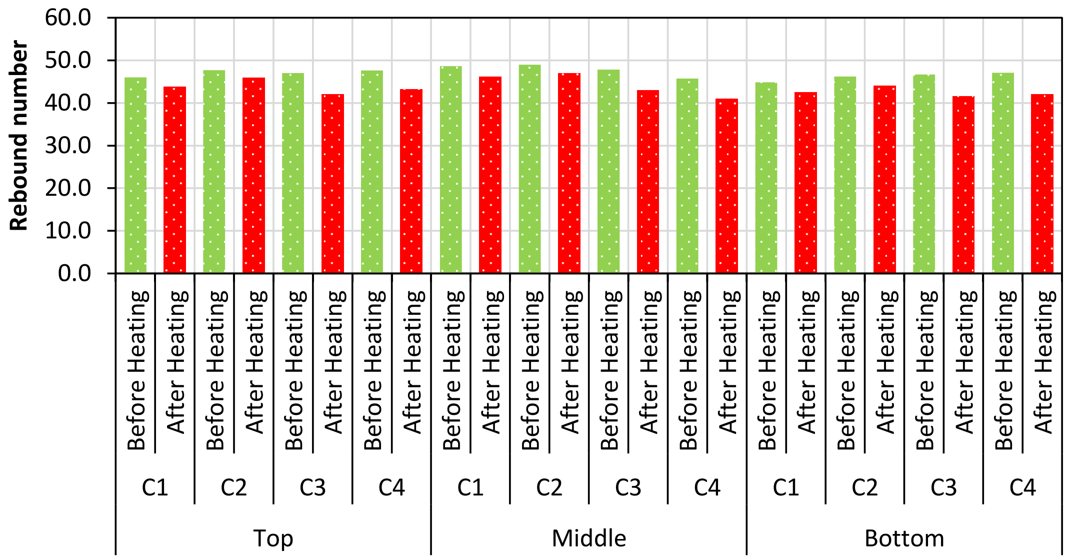

Figure 24. Rebound number of the specimens at three regions.

Following the UPV and rebound hammer tests, another test was performed, which was similar to the nondestructive evaluation. The natural frequency was determined, and the effect of dynamic characteristics was evaluated for the fire-affected specimens [53–55]. The natural frequency relies on the geometry and modulus of elasticity of a specific material. The natural frequency of a system is given in Equation (4).

$$\omega_n = \sqrt{\frac{k}{m}} \tag{4}$$

where ω_n is the natural frequency of the system (rad/s), k is the stiffness of the element (kN/m), and m is the mass of the element (kg).

Whenever there is structural damage, the stiffness is altered, which can eventually affect the dynamic characteristics. Ambient vibration measurements were performed to evaluate the dynamic characteristics of the heated and nonheated specimens. The schematic test arrangement is given in Figure 25. The column specimens were placed over a support that resembles a simply supported beam. A rubber mat was placed under the support to nullify the external vibrations.

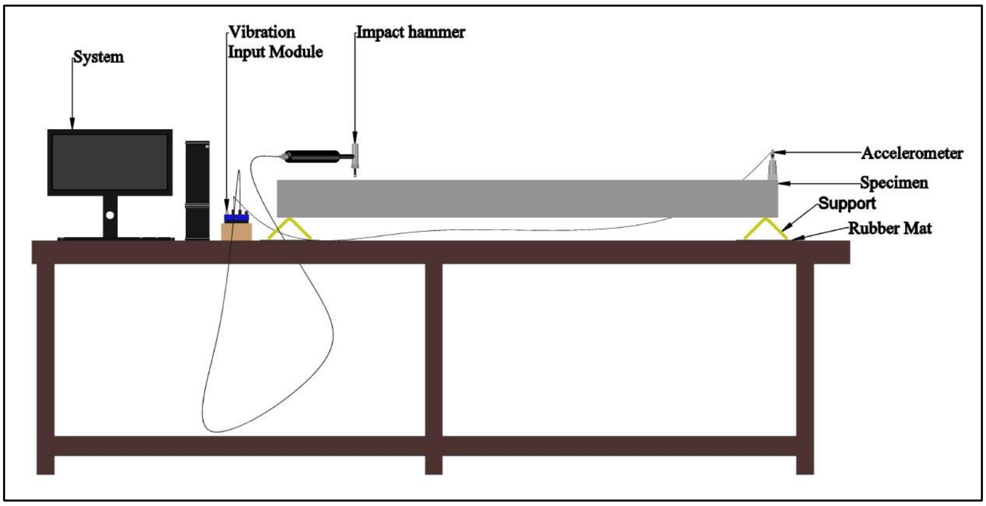

Figure 25. The schematic test arrangement for observing natural frequency.

The natural frequencies were measured every 50 mm through a span of 750 mm. The ambient vibrations were induced to the specimens through an impact hammer. A multipurpose accelerometer of sensitivity 100 mV/g was used to record the induced vibrations. The impact hammer and the accelerometer were coupled to the vibration input module, which helped in collecting the data, and the collected data were processed by the system.

The test arrangement of the specimens was shown in Figure 26. The input vibration signals were recorded for every corresponding stroke of the impact hammer. Similarly, the output signals were also captured. The typical pattern of recorded input and output signals for a specimen is shown in Figure 27.

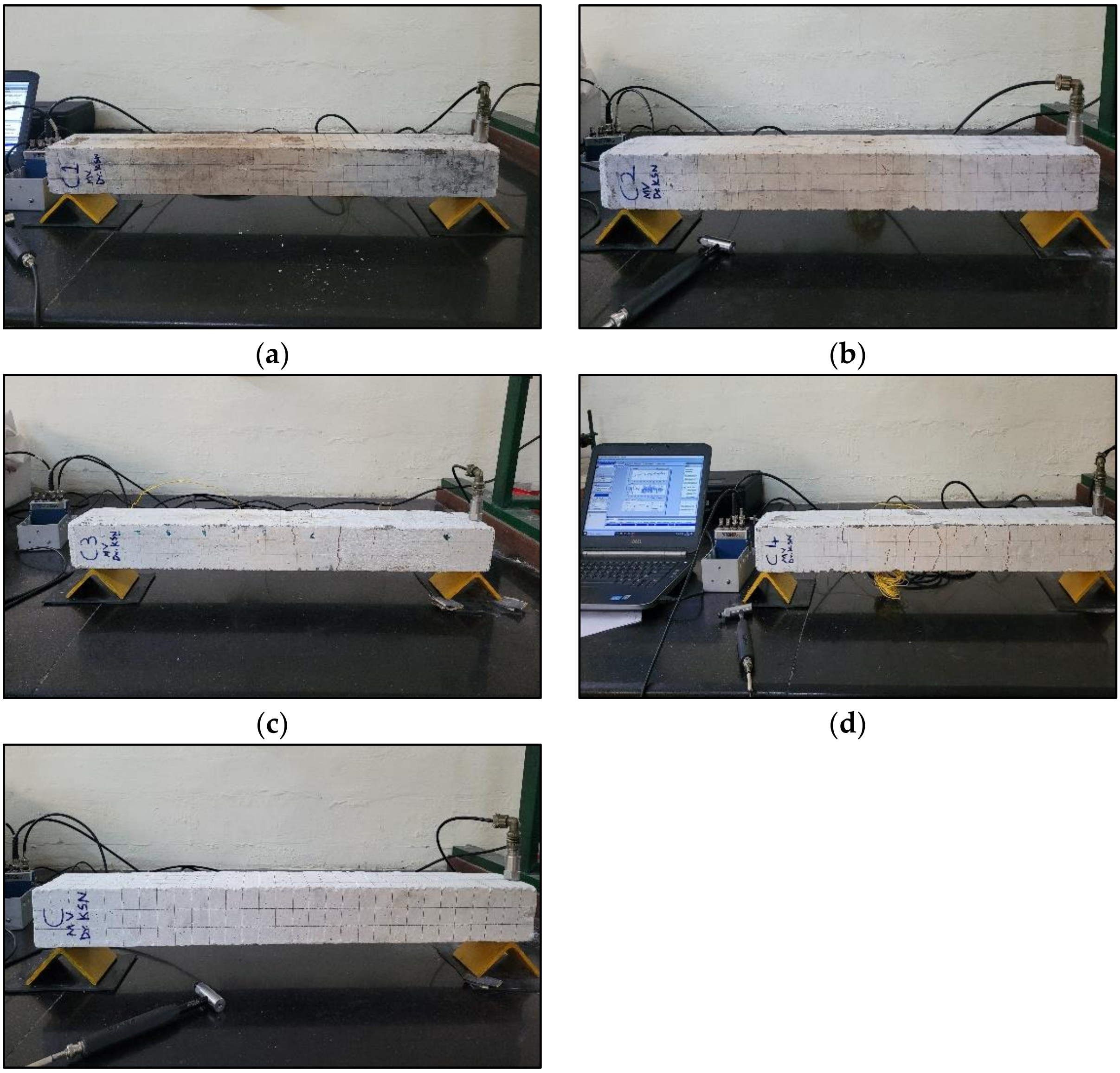

(**a**) (**b**) (**c**) (**d**) (**e**)

Figure 26. Test arrangement of specimens (**a**) C1, (**b**) C2, (**c**) C3, (**d**) C4, and (**e**) C.

In the observed magnitude, each peak represents a mode, and the first peak in the frequency represents a first mode. The natural frequency was observed in the first mode, and the observed natural frequency was plotted with respect to the height and is represented in Figure 28. Specimens C1 and C2 do not show any variation throughout the height. Specimens C, C3, and C4 show a great deal of variation throughout the height. This shows the intensity of fire damage in the specimens. The most fire-affected tested columns have a natural frequency of almost 90 Hz. The nonheated specimen has the lowest frequency range of 78-86 Hz. The least fire-affected specimens show a major variation throughout the height. This variation in natural frequency might be the effect of the presence of moisture content, which could act as a damping in nature. The effect of damping was estimated by calculating the damping ratio of the observed natural frequency of the specimens. The damping ratio was calculated using MATLAB.

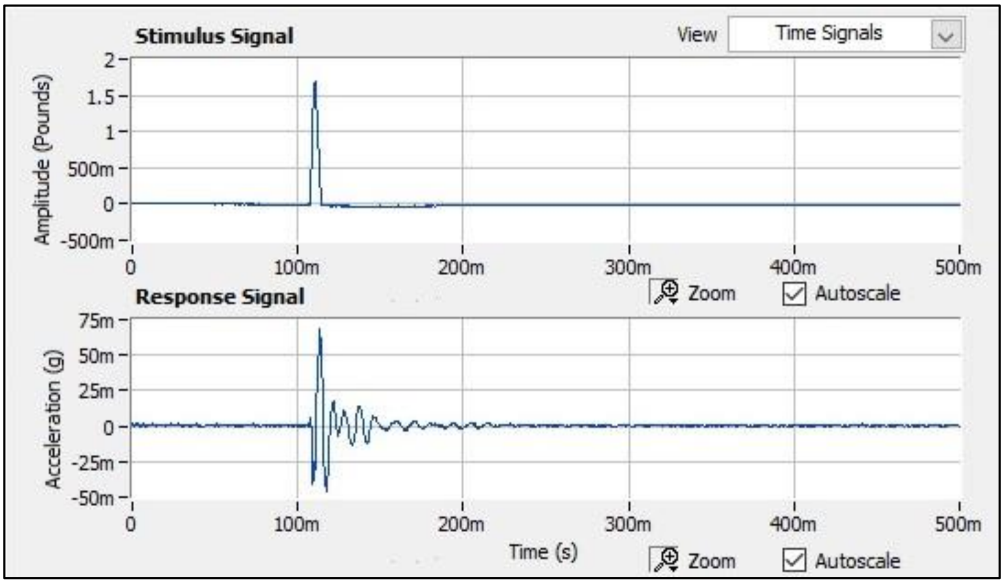

(**a**)

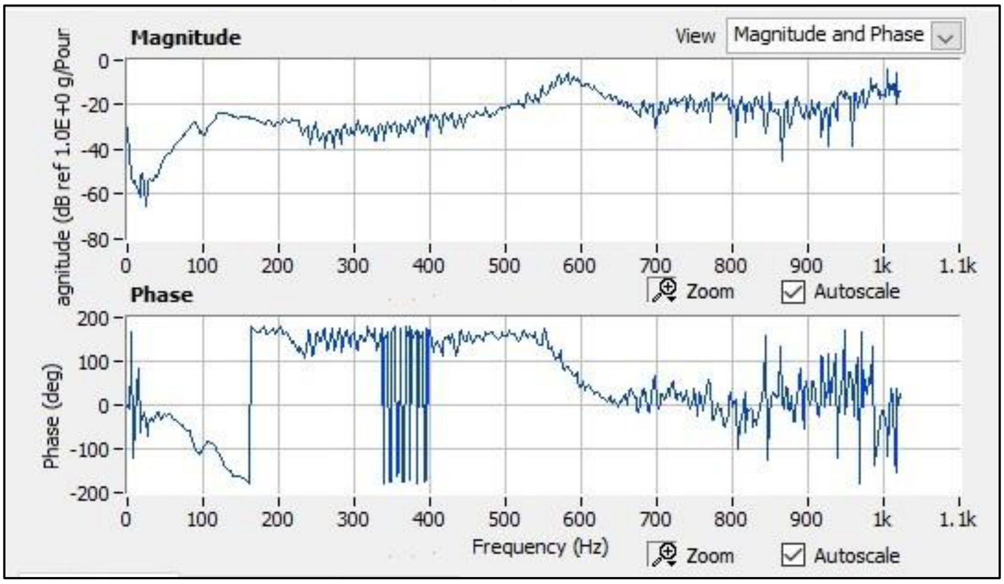

(**b**)

Figure 27. (**a**) Input signal. (**b**) Output signal.

The damping ratio is calculated by dividing the system's actual damping by its critical damping and it is given by Equation (5),

$$\zeta = \frac{C}{C_c} \tag{5}$$

The critical damping of a system is given by Equation (6),

$$C_c = 2m\omega_n \tag{6}$$

where ζ is the damping ratio of the system, C is the damping coefficient of the element, and C_c is the critical damping coefficient of the element.

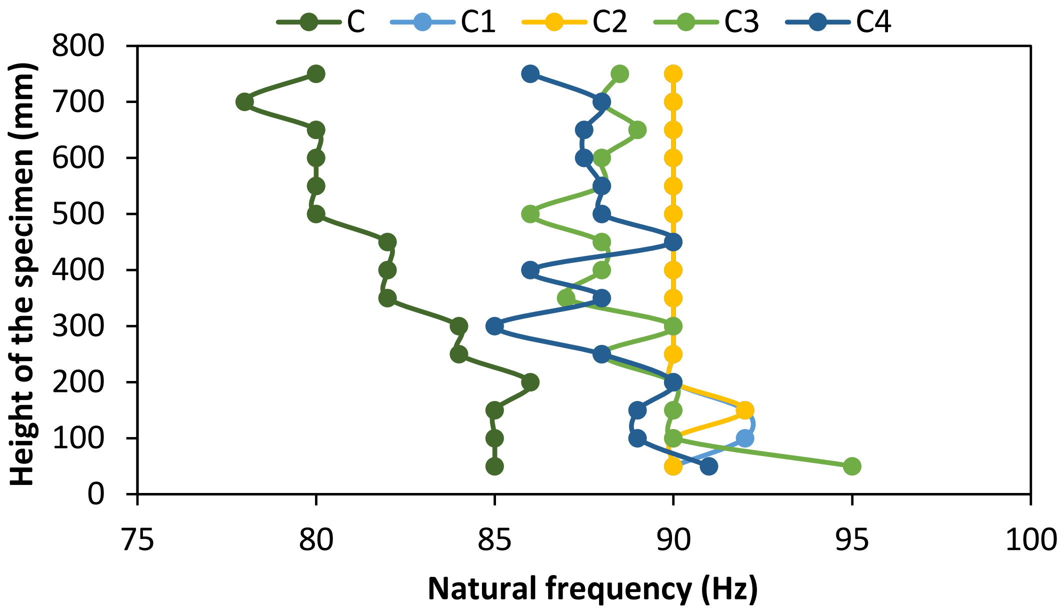

Figure 28. Observed natural frequency with respect to the height of the specimens.

The calculated damping ratios for the specimens are given in Figure 29. The overall calculated damping ratio was found to be less than 1, which falls under the category of an underdamped system. The damping ratio for the nonheated specimen was 0.1336. Among the heated specimens, specimen C4 has the highest damping ratio, and specimen C1 has the lowest damping ratio. This proves that the loss of moisture content was minimal while heating the specimens to the C4 condition. The faster heat transfer helps specimen C4 maintain its moisture content to a considerable level. This could significantly improve the stability of the column under seismic conditions, as it has a higher damping ratio than the other heated specimens. Specimen C4 could work effectively under the simultaneous action of fire and lateral loads or seismic loads.

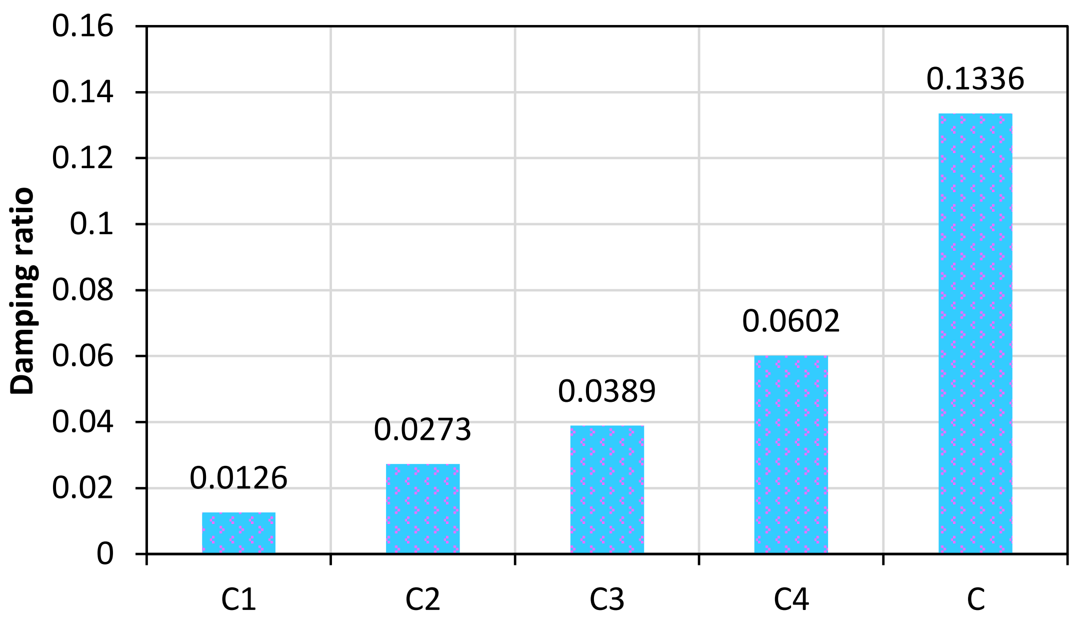

Figure 29. Damping ratio for the specimens.

5.6. Weight Loss in the Specimens after Heating

Similarly, the weight was observed, and weight loss was computed for the heated specimens to check the reduction in moisture content. The comparison of weight loss as a percentage between the specimens is shown in Figure 30.

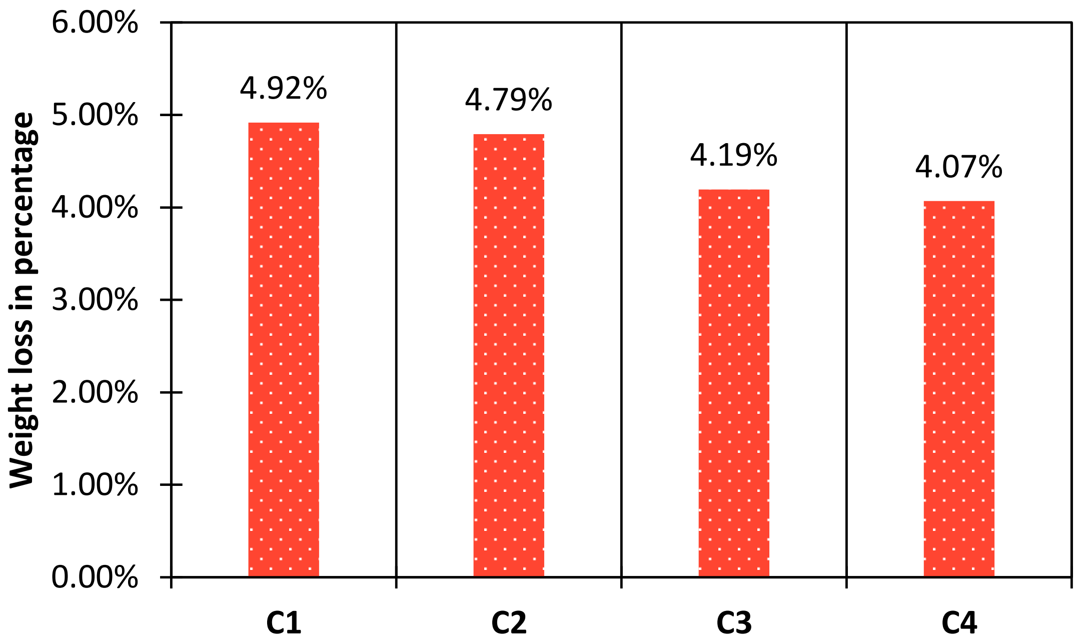

Figure 30. Percentage of weight loss in the specimens.

Generally, while heating, the concrete elements undergo severe loss in their moisture content. The moisture content present inside the concrete tries to escape due to the heat. The existence of moisture content plays a crucial role in the stability of the concrete structural element. After heating, the most heat-dissipated columns C4 and C3 had the lowest reduction in weight after heating compared to C2. Specimen C4 has the lowest reduction in weight loss percentage, which was 17.3% less than that of specimen C1. This shows that the better heat-dissipating specimens help to maintain the moisture content present inside the concrete. The existence of sufficient moisture content ultimately prevents the bursting of concrete under high temperatures.

5.7. X-ray of the Specimens

All specimens were visualized under X-rays to find the internal damage. For the purpose of X-ray, the top cone of the specimen was removed and visualized separately. Specimens C1 and C2 seem to have more white patches throughout the height, while specimens C, C4, and C3 have more black patches throughout the height. This moisture content is present inside. The loss of moisture content can be seen through the white patches in specimens C1 and C2. The presence of moisture content can be visualized through the black patches in specimens C, C4, and C3. The X-ray over the cone regions also summarizes the same as the cones from specimens C3 and C4, which have more black patches than the cone of specimen C2. The X-ray images of the specimens are represented in Figure 31.

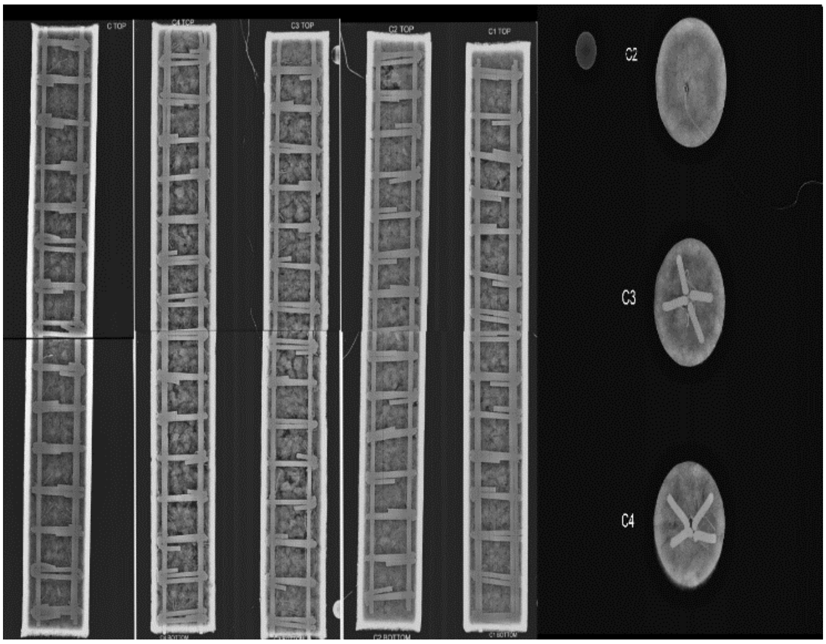

Figure 31. X-ray images of the column specimens.

5.8. Ultimate Load Capacity of the Columns

The column specimens were tested in a Universal Testing Machine with a capacity of 1000 kN to determine the ultimate load capacity. The deflection readings were gauged at the top, middle, and bottom regions using a dial gauge with a capacity of 100 mm. Regional strains were computed at the top, middle, and bottom regions using a demec gauge. The test arrangement of the specimens with the entire setup before testing is represented in Figure 32.

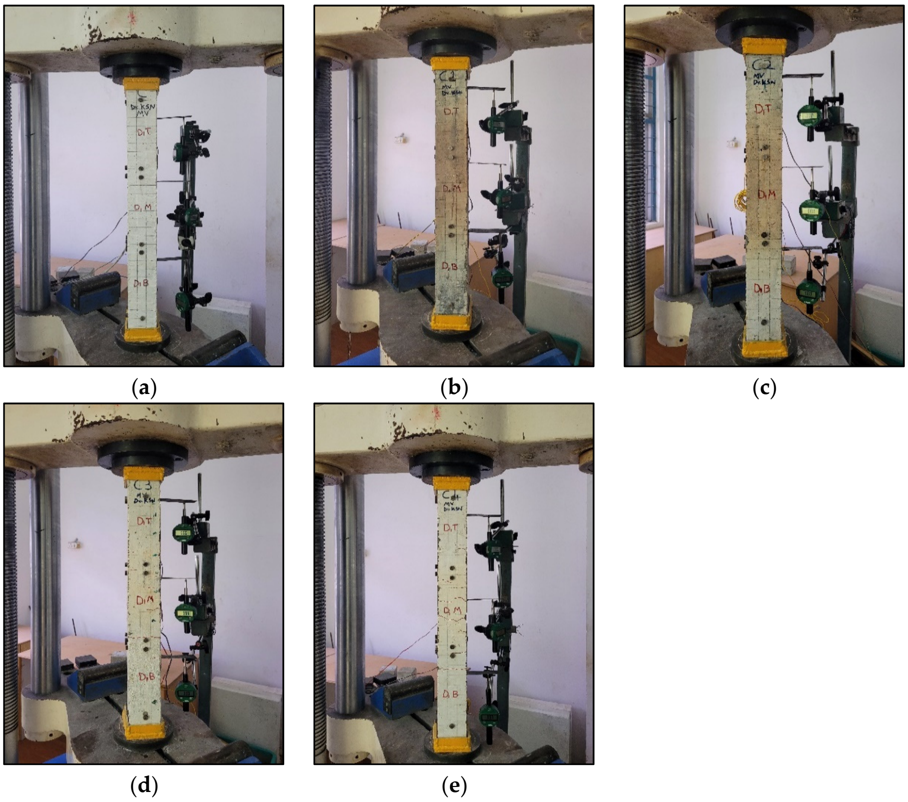

Figure 32. Entire test setup of specimens (**a**) C, (**b**) C1, (**c**) C2, (**d**) C3, and (**e**) C4.

The deformation of the column was observed at the top, middle, and bottom regions and was plotted against the load. The load versus deformation profile of the top, middle, and bottom regions are exhibited in Figure 33. The crack pattern was noticed after the ultimate load. The crack patterns of the specimens after testing are exhibited in Figure 34.

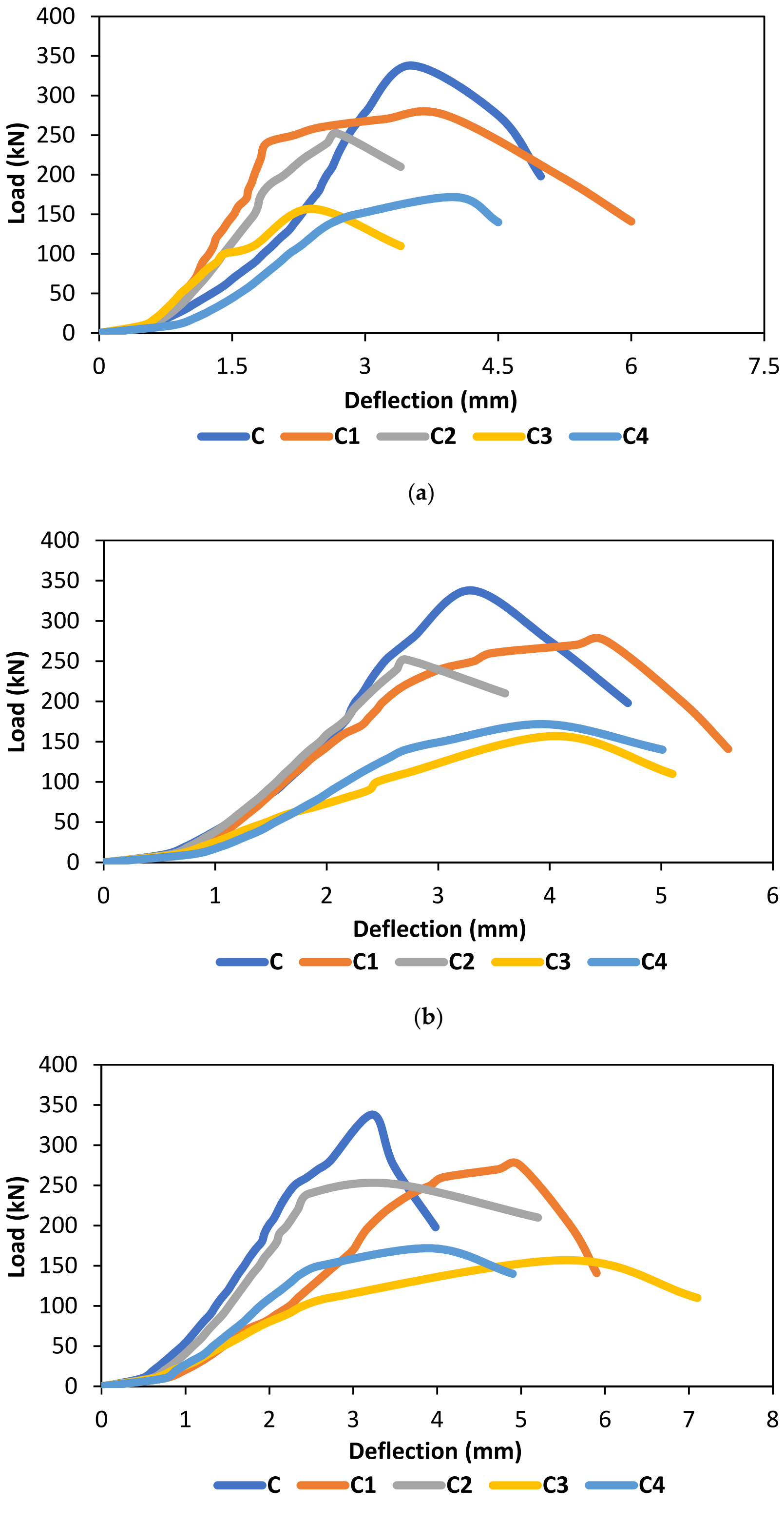

Figure 33. Load versus deformation profile of the specimens: (**a**) Top, (**b**) Middle, and (**c**) Bottom.

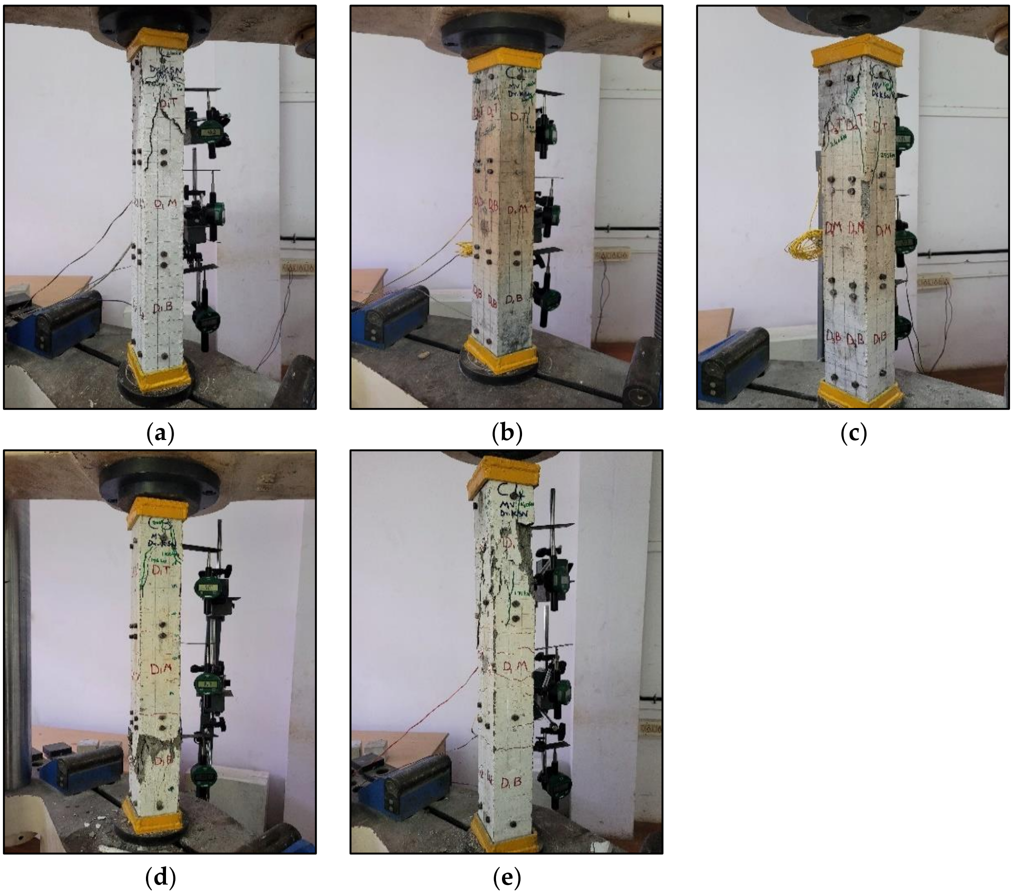

Figure 34. Crack pattern of the specimens after testing (**a**) C, (**b**) C1, (**c**) C2, (**d**) C3, and (**e**) C4.

5.9. Initial and Final Cracking Loads

The initial cracking load and the ultimate load were noticed and are represented in Figure 35. The nonheated specimen reached a maximum ultimate load of 338 kN. The initial cracks were developed at a load of 250 kN. Quenched specimen C4 starts to crack at a load of 130 kN and attains a maximum load of 171.7 kN. The cracks on the conventional heated specimen C1 started to develop at a load of 170 kN and attained a maximum load of 275.55 kN. The strength of the most heat-dissipated columns was reduced. The reduction in strength was noticed in the evaluation of the rebound hammer.

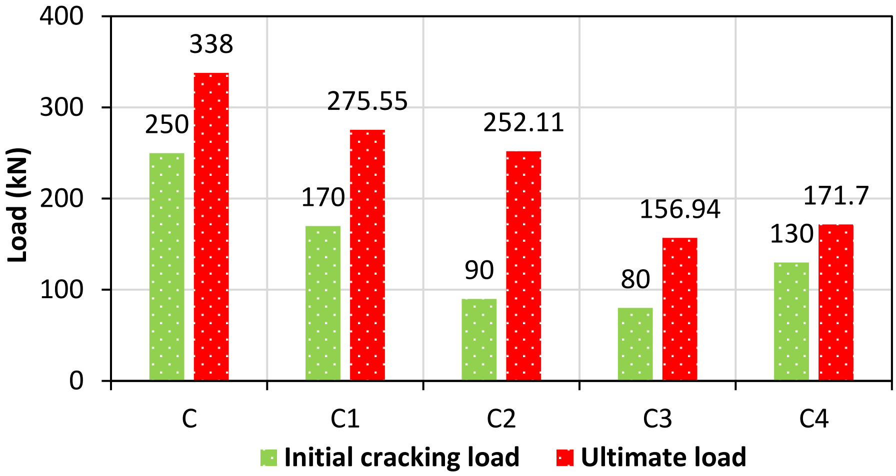

Figure 35. Initial cracking load and ultimate load of the specimens.

The difference in percentage between the initial and final cracking loads was calculated and is represented in Figure 36.

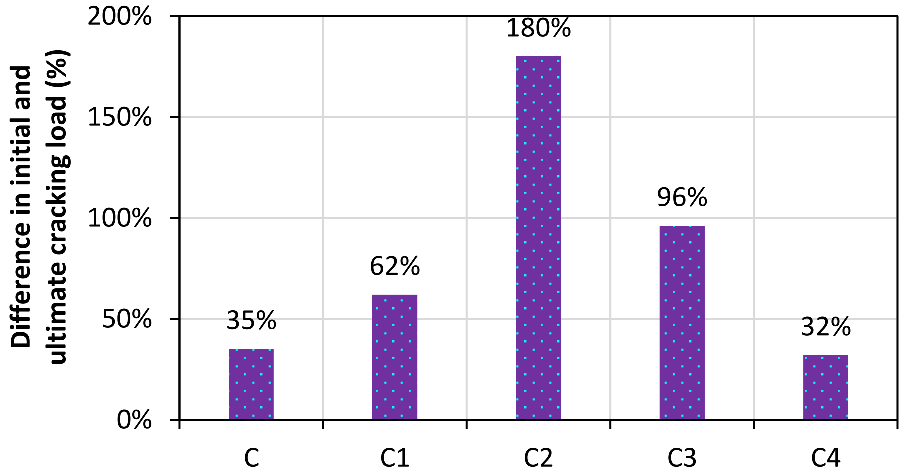

Figure 36. Difference in percentage between the initial and final cracking load of the specimens.

The nonheated specimen and specimen C4 follow a similar trend in the difference between the initial and final cracking loads. This shows that the ultimate failure is predictable within a shorter duration from the occurrence of the initial crack. Specimens C1, C2, and C3 will be unreliable in predicting failure, as it may occur at any time during the post-fire scenario.

5.10. Stiffness of the Specimens

Based on the ultimate load and deformation, the stiffness was calculated and is represented in Figure 37.

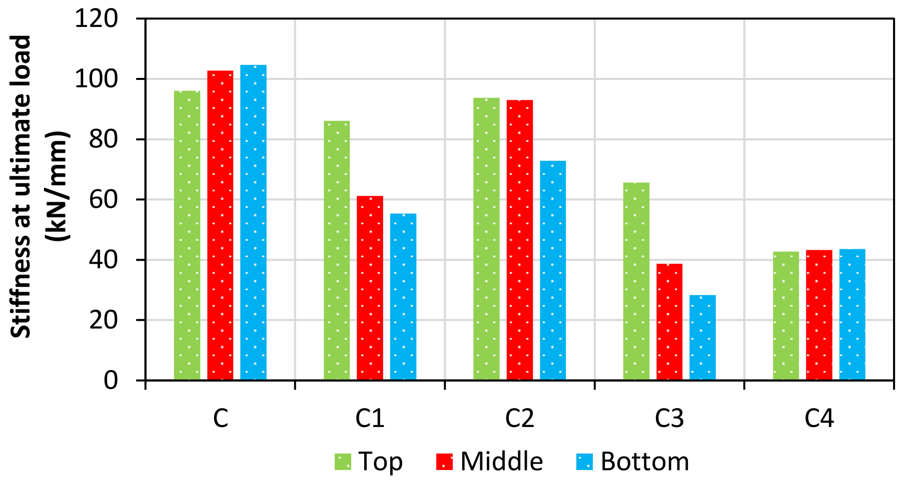

Figure 37. Stiffness of the specimens at the top, middle, and bottom regions.

The nonheated column is almost uniform throughout the height. The differential heating condition created a nonuniform stiffness throughout the height of the heated column except for specimen C4. The stiffness of specimen C4 is similar to that of the nonheated column. Quantitatively, the stiffness of specimen C4 was less but followed a similar trend. The quenching effect reduces the overall stiffness but helps in distributing the temperature throughout the height, which subsequently maintains the uniform stiffness [56,57]. The failure of the specimens can be easily predicted for specimens that have uniform stiffness rather than nonuniform stiffness. This nonuniform stiffness could affect the stability of the column in the postfire condition.

5.11. Modulus of Elasticity of the Specimens

The modulus of elasticity was calculated based on the observed regional strain values and is represented in Figure 38. Specimens C and C4 follow a similar trend by maintaining almost equal values in the three regions. The other specimens have uneven modulus values over the regions. The case was similar to the stiffness of the columns in three regions. Although the modulus values were lower in C4, it has a uniform modulus, similar to that of specimen C. This again proves the uniform strength reduction throughout the height of the column.

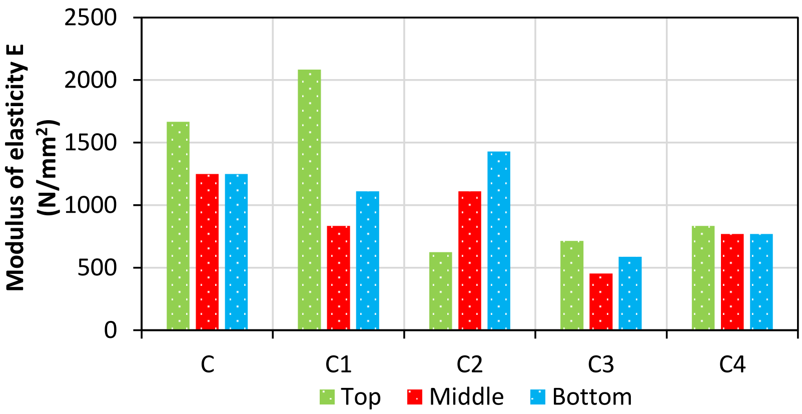

Figure 38. Modulus of elasticity of the specimens at the top, middle, and bottom regions.

Using the resulting modulus of elasticity values, the unequal stiffness decrease was quantitatively validated. For the related numerical validation, a prototype model identical to that described in Section 2 was utilized. The specimens C1 and C4's moduli of elasticity were verified numerically. The portion of the column was divided into the top, middle, and bottom, and their respective modulus of elasticity values were integrated. A 100 kN load was placed to the top of the column, and the supports were designated as pinned. After simulation, the stress was taken into consideration at 200 mm intervals along the whole height of the column. Figure 39 depicts the stress pattern created along the height of column specimens C1 and C4, whereas Figure 40 depicts the comparison of stress along the height of the specimen C1 and C4.

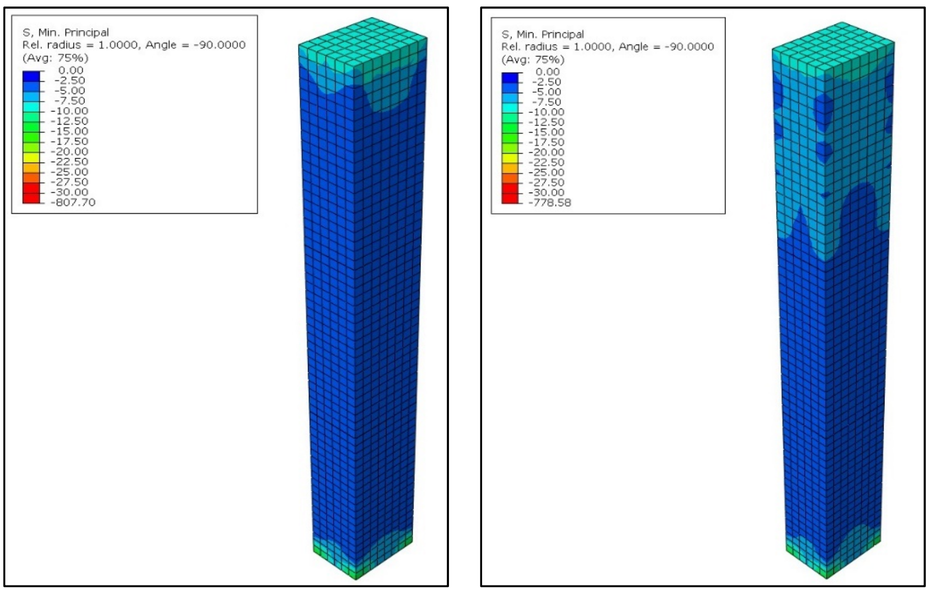

(**a**) (**b**)

Figure 39. Stress pattern formed along the height of the column (**a**) C4, (**b**) C1.

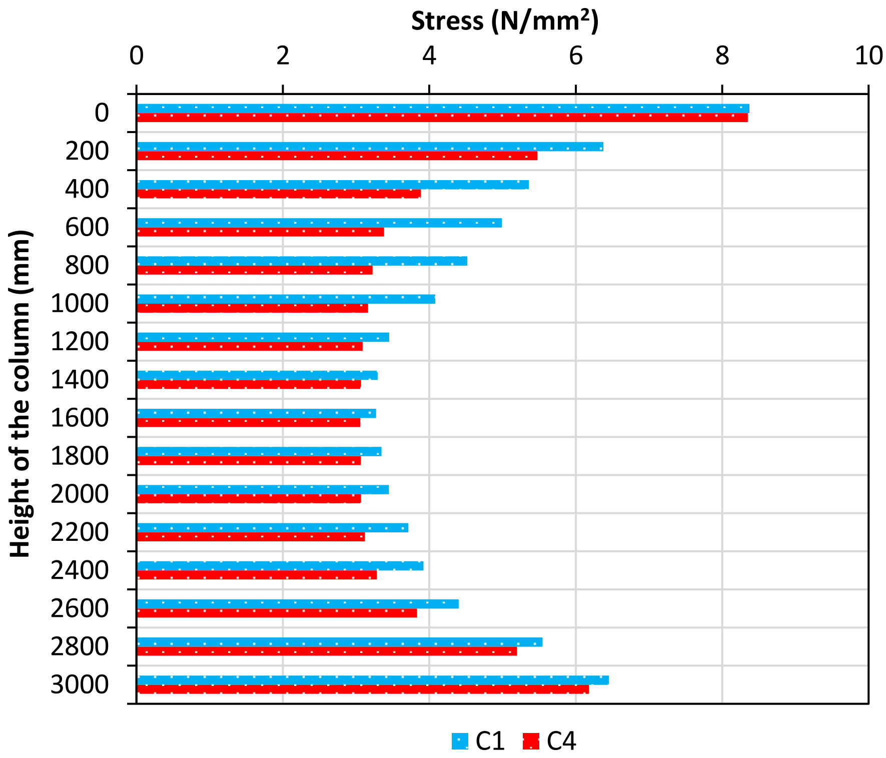

Figure 40. Comparison of stress along the height of the column.

Specimen C4 shows stress that is nearly consistent over the entirety of its central region. The specimen C4 experienced less stress than the specimen C1. This validates the impact of homogeneous column stiffness across its height. The stability of the mimicked column (C4) during high fire conditions is ensured by its lower stress intensity than that of the conventional column (C1). This might save the building from a catastrophic fire without any extensive fire-resistant measures.

6. Conclusions

This study presents the self-heat-dissipating nature of reinforced concrete columns under fire scenarios through biomimicry of a cactus plant. Cactus plants have the unique feature of sustaining hot dry weather by dissipating heat through sharp pointed spikes. The conventional fire protection and resistance technique incorporates another material that eventually increases the cost. The proposed geometry was made up of the same concrete, where only the top geometry was altered to dissipate the heat. To evaluate the heat dissipation, different geometries were considered, and the better heat-dissipating geometry was optimized through finite element analysis. The optimized geometry was tested experimentally to understand the heat dissipation nature. Furthermore, the structural parameters were observed to understand the postfire stability of the column. The following are the key findings of this study:

- The mimicked specimens show a better heat dissipation nature than the conventional specimen. The rate of cooling was faster in the quenched specimen.
- The quenched specimen undergoes more thermal elongation and contraction as a result of faster heat dissipation; as a result, it generates more cracks on the better heat dissipated specimens.
- The dynamic analysis proved to be one the best structural health monitoring technique and nondestructive testing evaluation method, as the results were found to be satisfactory in the case of fire damage evaluation.
- From the dynamic analysis, the damping ratio of the quenched specimen was reclaimed to be higher than that of the other heated specimens. The damping ratio of the quenched specimen was higher than that of the conventional heated specimen. This

eventually shows the intensity of fire damage and the presence of moisture content inside. The X-ray images also prove the presence of moisture content, and they were in good covenant with the results of dynamic analysis.

- The ultimate load of the quenched specimen was found to be less than that of the conventional heated and nonheated specimen, as the quenching effect reduces the overall load-carrying capacity of the column.
- The stiffness of the columns at different regions shows major variation except for the quenched and nonheated column. The quenching effect helps the member maintain its stiffness at almost the same level over the height. Although the stiffness was quantitatively less than that of the nonheated specimen, they followed the same trend. This could eventually prevent the uneven collapse of the member under localized fire conditions.
- The modulus of elasticity calculated at the regions also shows that the quenched specimen maintains uniform strength throughout the height, similar to that of the nonheated specimen.

The biomimicked geometries act as a self-heat-dissipating system that eventually protects the column under fire breakout without any external application. A structural member maintaining a uniform strength through its height after localized fire conditions is a key aspect in preventing the global collapse of a structure. This eventually maintains the stability of the structure under the postfire scenario. The proposed geometry could be implemented in an existing structural member, which is one of the major concerns.

7. Patents

An Indian patent was published from this research work under the title "Reinforced Concrete Column for Controlling Temperature under Fire Breakout Using Geometry Biomimicking" on 23/09/2022. Patent publication no. 202241053085.

Author Contributions: Conceptualization, S.K.S.; Validation, S.K.S.; Investigation, M.V.; Data curation, M.V.; Writing—original draft, M.V.; Writing—review & editing, M.V. All authors have read and agreed to the published version of the manuscript.

Funding: This research received no external funding.

Data Availability Statement: Not applicable.

Acknowledgments: We acknowledge the Machine Dynamics Laboratory in Department of Mechanical Engineering, SRMIST for providing the support towards Dynamic Analysis and Structural Testing Laboratory in Department of Civil Engineering, SRMIST for offering tremendous support towards testing.

Conflicts of Interest: The authors declare no conflict of interest.

References

1. Ma, Z.; Shen, J.; Wang, C.; Wu, H. Characterization of sustainable mortar containing high-quality recycled manufactured sand crushed from recycled coarse aggregate. *Cem. Concr. Compos.* **2022**, *132*, 104629. [CrossRef]
2. Ahamed, M.K.; Wang, H.; Hazell, P.J. From biology to biomimicry: Using nature to build better structures—A review. *Constr. Build. Mater.* **2022**, *320*, 126195. [CrossRef]
3. Oguntona, O.A.; Aigbavboa, C.O. Biomimetic reinvention of the construction industry: Energy management and sustainability. *Energy Procedia* **2017**, *142*, 2721–2727. [CrossRef]
4. Charkas, M.N. Towards Environmentally Responsive Architecture: A Framework for Biomimic Design of Building'S Skin. *JES J. Eng. Sci.* **2019**, *47*, 371–388. [CrossRef]
5. Gorb, S.N.; Gorb, E.V. Insect-inspired architecture to build sustainable cities. *Curr. Opin. Insect Sci.* **2020**, *40*, 62–70. [CrossRef]
6. Grigorian, M. Biomimicry and theory of structures-design methodology transfer from trees to moment frames. *J. Bionic Eng.* **2014**, *11*, 638–648. [CrossRef]
7. Yiatros, S.; Wadee, M.A.; Hunt, G.R. The load-bearing duct: Biomimicry in structural design. *Proc. Inst. Civ. Eng. Eng. Sustain.* **2007**, *160*, 179–188. [CrossRef]
8. Hu, Z.; Thiyagarajan, K.; Bhusal, A.; Letcher, T.; Fan, Q.H.; Liu, Q.; Salem, D. Design of ultra-lightweight and high-strength cellular structural composites inspired by biomimetics. *Compos. Part B Eng.* **2017**, *121*, 108–121. [CrossRef]

9. Soltan, D.G.; Ranade, R.; Li, V.C. A Bio-inspired Cementitious Composite for High Energy Absorption in Infrastructural Applications. *Blucher Mater. Sci. Proc.* **2014**, *1*, 1–4. [CrossRef]
10. Nachiar, S.S.; Satyanarayanan, K.S.; Lakshmipathy, M.; Pavithra, S.S. Study on behaviour of compression members based on concept of biomimics. *Mater. Today Proc.* **2018**, *34*, 518–524. [CrossRef]
11. Nachiar, S.S.; Satyanarayanan, K.S.; Lakshmipathy, M. Study on the behaviour of tension member based on the concept of biomimics. *Mater. Today Proc.* **2018**, *34*, 371–378. [CrossRef]
12. Nachiar, S.S.; Satyanarayanan, K.S.; Lakshmipathy, M. Experimental investigation on the behavior of biomimicked columns subjected to compression. *Int. J. Civ. Eng. Technol.* **2018**, *9*, 771–778.
13. Nachiar, S.S.; Shilpa, P.; Satyanarayanan, K.S.; Anandh, S. Modeling and analysis of a pin jointed plane frame using Biomimicked structural elements. *Mater. Today Proc.* **2021**, *50*, 259–268. [CrossRef]
14. Abed, M.S.; Resan, S.F.; Zemam, S.K. Developing knotted slender reinforced concrete column based on bamboo culm biomimicry. *Asian J. Civ. Eng.* **2022**, *23*, 99–111. [CrossRef]
15. Kaluvan, S.; Park, C.Y.; Choi, S.B. Bio-inspired device: A novel smart MR spring featuring tendril structure. *Smart Mater. Struct.* **2015**, *25*, 01LT01. [CrossRef]
16. Fan, J.; He, J.H. Biomimic design of multi-scale fabric with efficient heat transfer property. *Therm. Sci.* **2012**, *16*, 1349–1352. [CrossRef]
17. Reichert, S.; Menges, A.; Correa, D. Meteorosensitive architecture: Biomimetic building skins based on materially embedded and hygroscopically enabled responsiveness. *CAD Comput. Aided Des.* **2015**, *60*, 50–69. [CrossRef]
18. Mathews, M.E.; Kiran, T.; Anand, N.; Lubloy, E.; Naser, M.Z.; Arulraj, G.P. Effect of protective coating on axial resistance and residual capacity of self-compacting concrete columns exposed to standard fire. *Eng. Struct.* **2022**, *264*, 114444. [CrossRef]
19. Li, Y.; Du, P.; Tan, K.H. Fire resistance of ultra-high performance concrete columns subjected to axial and eccentric loading. *Eng. Struct.* **2021**, *248*, 113158. [CrossRef]
20. Xu, L.; Bao, Y.H. Experimental study on the fire resistance of concrete filled steel tube reinforced concrete (CFSTRC) column-RC beam frames. *Adv. Struct. Eng.* **2021**, *24*, 2413–2426. [CrossRef]
21. Yang, D.; Liu, F.; Huang, S.-S.; Yang, H. Structural fire safety design of square and rectangular tubed-reinforced-concrete columns. *Structures* **2020**, *29*, 1286–1321. [CrossRef]
22. Wen, B.; Zhang, L.; Wu, B.; Niu, D.; Wang, L.; Zhang, Y. Fire resistance of earthquake damaged reinforced concrete columns. *Struct. Infrastruct. Eng.* **2021**, *18*, 1–23. [CrossRef]
23. Du, P.; Yang, Y.; Tan, K.H. Fire behaviour and design of hybrid fibre reinforced high-performance concrete columns subjected to uniaxial bending. *Eng. Struct.* **2022**, *251*, 113425. [CrossRef]
24. Chen, Z.; Liao, H.; Zhou, J.; Ye, P. Eccentric compression behavior of reinforced recycled aggregate concrete columns after exposure to elevated temperatures: Experimental and numerical study. *Structures* **2022**, *43*, 959–976. [CrossRef]
25. Gernay, T. Fire resistance and burnout resistance of reinforced concrete columns. *Fire Saf. J.* **2019**, *104*, 67–78. [CrossRef]
26. Tan, K.H.; Yao, Y. Fire Resistance of Four-Face Heated Reinforced Concrete Concrete Columns. *Beton-Und Stahlbetonbau* **2003**, *103*, 472–481. [CrossRef]
27. Buch, S.H.; Sharma, U.K. Statistical Review of the Fire Resistance of Concrete Columns. *Arab. J. Sci. Eng.* **2022**. [CrossRef]
28. Naser, M.Z.; Kodur, V.K. Explainable machine learning using real, synthetic and augmented fire tests to predict fire resistance and spalling of RC columns. *Eng. Struct.* **2022**, *253*, 113824. [CrossRef]
29. Buch, S.H.; Sharma, U.K. Empirical model for determining fire resistance of Reinforced Concrete columns. *Constr. Build. Mater.* **2019**, *225*, 838–852. [CrossRef]
30. Bajc, U.; Kolšek, J.; Planinc, I.; Bratina, S. Fire resistance of RC columns with regard to spalling of concrete. *Fire Saf. J.* **2022**, *130*, 103568. [CrossRef]
31. Yu, M.; Hu, X.; Xu, L.; Cheng, S. A general unified method for calculating fire resistance of CFST columns considering various types of steel and concrete. *J. Build. Eng.* **2022**, *59*, 105125. [CrossRef]
32. Rahnavard, R.; Craveiro, H.D.; Simões, R.A.; Laím, L.; Santiago, A. Fire resistance of concrete-filled cold-formed steel (CF-CFS) built-up short columns. *J. Build. Eng.* **2021**, *48*, 103854. [CrossRef]
33. Fellouh, A.; Bougara, A.; Piloto, P.; Benlakehal, N. Fire resistance of partially encased composite columns subjected to eccentric loading. *J. Struct. Fire Eng.* **2022**, *13*, 451–469. [CrossRef]
34. Shao, Z.; Zha, X.; Wan, C. Design method of fire-resistance capacity of reinforced-concrete-filled steel tube column under axial compression. *Fire Saf. J.* **2022**, *129*, 103572. [CrossRef]
35. Kong, W.; Fu, C.; Liu, W. Study on the Deformation Behaviour of Reinforced Concrete Beam-Supporting Column Transfer Structures during Fire Exposure. *KSCE J. Civ. Eng.* **2022**, *26*, 2765–2779. [CrossRef]
36. Possidente, L.; Weiss, A.; de Silva, D.; Pustorino, S.; Nigro, E.; Tondini, N. Fire safety engineering principles applied to a multi-storey steel building. *Proc. Inst. Civ. Eng. Struct. Build.* **2021**, *174*, 725–738. [CrossRef]
37. Santarpia, L.; Bologna, S.; Ciancio, V.; Golasi, I.; Salata, F. Fire temperature based on the time and resistance of buildings—predicting the adoption of fire safety measures. *Fire* **2019**, *2*, 19. [CrossRef]
38. Mullins-jaime, C.; Smith, T.D. Nanotechnology in Residential Building Materials for Better Fire Protection and Life Safety Outcomes. *Fire* **2022**, *5*, 174. [CrossRef]

39. van Coile, R.; Hopkin, D.; Elhami-Khorasani, N.; Gernay, T. Demonstrating adequate safety for a concrete column exposed to fire, using probabilistic methods. *Fire Mater.* **2021**, *45*, 918–928. [CrossRef]
40. Parthasarathi, N.; Satyanarayanan, K.S.; Prakash, M.; Farsangi, E.N.; Thirumurugan, V.; Srinivasasenthil, S. Progressive collapse evaluation of RC frames under high-temperature conditions: Experimental and finite element investigations. *Structures* **2022**, *41*, 375–388. [CrossRef]
41. Wickström, U. *Temperature Calculation in Fire Safety Engineering*; Springer Nature: Berlin, Germany, 2016. [CrossRef]
42. Chetti, M.B.; Nobel, P.S. Recovery of photosynthetic reactions after high-temperature treatments of a heat-tolerant cactus. *Photosynth. Res.* **1988**, *18*, 277–286. [CrossRef]
43. Lewis, D.A.; Nobel, P.S. Thermal Energy Exchange Model and Water Loss of a Barrel Cactus, Ferocactus acanthodes. *Plant Physiol.* **1977**, *60*, 609–616. [CrossRef] [PubMed]
44. Walker, L.R. The Saguaro Cactus: A Natural History. By David Yetman, Alberto Búrquez, Kevin Hultine, and Michael Sanderson. *West. Hist. Q.* **2020**, *51*, 487–488. [CrossRef]
45. IS 456. Concrete, Plain and Reinforced. *Bur. Indian Stand. Dehli* **2000**, 1–114.
46. Vishal, M.; Satyanarayanan, K.; Thirumurugan, V. Analytical investigation on behavior of three-dimensional reinforced concrete frames under thermal effect. *Mater. Today: Proc.* **2021**, *50*, 248–252. [CrossRef]
47. Murugan, V.; Srinivasan, S.K. Influence of cover thickness in structural frames exposed to fire and service loads. *Environ. Sci. Pollut. Res.* **2021**, *29*, 85955–85968. [CrossRef]
48. Vishal, M.; Satyanarayanan, K.S. Analytical Investigation on Progressive Collapse of 3-D Reinforced Concrete Frames under High Temperature. In *Resilient Infrastructure*; Springer: Singapore, 2022; pp. 269–279.
49. Cuong-Le, T.; le Minh, H.; Sang-To, T. A nonlinear concrete damaged plasticity model for simulation reinforced concrete structures using ABAQUS. *Frat. ed Integrita Strutt.* **2021**, *16*, 232–242. [CrossRef]
50. EN 1991-1-7. Eurocode 1—Action on structures—Part 1–7: General actions—Accidental actions. *Eur. Comm. Stand.* **2006**, *54*, 18–20. [CrossRef]
51. *ISO 834-11*; Fire Resistance Tests—Elements of Building Construction. Part 11 Specif. Requir. Assess. Fire Prot. to Strucutral Steel Elem. ISO: Geneva, Switzerland, 2014.
52. Usmani, A.S.; Rotter, J.M.; Lamont, S.; Sanad, A.M.; Gillie, M. Fundamental principles of structural behaviour under thermal effects. *Fire Saf. J.* **2001**, *36*, 721–744. [CrossRef]
53. Singh, T.; Sehgal, S.; Prakash, C.; Dixit, S. Real-Time Structural Health Monitoring and Damage Identification Using Frequency Response Functions along with Finite Element Model Updating Technique. *Sensors* **2022**, *22*, 4546. [CrossRef]
54. Pranno, A.; Greco, F.; Lonetti, P.; Luciano, R.; de Maio, U. An improved fracture approach to investigate the degradation of vibration characteristics for reinforced concrete beams under progressive damage. *Int. J. Fatigue* **2022**, *163*, 107032. [CrossRef]
55. Altunişik, A.C.; Akbulut, Y.E.; Başağa, H.B.; Mostofi, S.; Mosallam, A.; Wafa, L.F. Experimental Investigation on Dynamic Characteristics Changes of Fire Exposed Reinforced Concrete and Steel Members. *Fire Technol.* **2021**, *58*, 1169–1208. [CrossRef]
56. Pul, S.; Atasoy, A.; Senturk, M.; Hajirasouliha, I. Structural performance of reinforced concrete columns subjected to high-temperature and axial loading under different heating-cooling scenarios. *J. Build. Eng.* **2021**, *42*, 102477. [CrossRef]
57. Li, Y.; Yang, E.H.; Tan, K.H. Effects of heating followed by water quenching on strength and microstructure of ultra-high performance concrete. *Constr. Build. Mater.* **2019**, *207*, 403–411. [CrossRef]